recycling

MDPI

Article

Valorization of Pb–Zn Mine Waste in Metakaolin-Based Geopolymers: A Circular Approach for Waste Reuse and Methylene Blue Removal

Jihene Nouairi [1,2,3,*], Slávka Andrejkovičová [4], Oumaima Karoui [5], Tiago Pinho [4], Rafael Rebelo [4], Gil Gonçalves [6,7], Angelo Camerlenghi [1], Mounir Ghribi [1] and Fernando Rocha [4]

1 National Institute of Oceanography and Applied Geophysics—OGS, Borgo Grotta Gigante 42/C, 34010 Trieste, Italy; acamerlenghi@ogs.it (A.C.); mghribi@ogs.it (M.G.)
2 International Centre for Theoretical Physics—ICTP, Strada Costiera, 11, 34151 Trieste, Italy
3 Centre of Excellence for Sustainable Blue Economy and Ocean Governance, EMUNI University, Pristaniška ulica 14, 6000 Koper, Slovenia
4 Geosciences Department, Geobiotec Research Unit, University of Aveiro, Campus Universitário de Santiago, 3810-193 Aveiro, Portugal; slavka@ua.pt (S.A.); tiagoapinho@ua.pt (T.P.); rafa.rebelo@ua.pt (R.R.); tavares.rocha@ua.pt (F.R.)
5 Georessources Laboratory, Centre de Recherches et des Technologies des Eaux (CERTE), Soliman 273-8020, Tunisia; omaima.karoui@fst.utm.tn
6 TEMA—Centre for Mechanical Technology and Automation, Department of Mechanical Engineering, University of Aveiro, 3810-193 Aveiro, Portugal; ggoncalves@ua.pt
7 Intelligent Systems Associate Laboratory (LASI), 4800-058 Guimarães, Portugal
* Correspondence: jnouairi@ogs.it; Tel.: +39-3519944398

Abstract

The increasing accumulation of mine waste and the associated release of toxic elements represent a major environmental challenge, particularly in regions impacted by Pb–Zn mining activities. In this context, this study aims to investigate the valorization of mine waste from Lakhouat, an abandoned Pb–Zn site in Northern Tunisia, as a sustainable additive in metakaolin-based geopolymers. This approach contributes to circular economy strategies by transforming hazardous waste into value-added materials for environmental and construction applications. Geopolymer formulations were synthesized by incorporating mine waste at different proportions (0, 5, 10, 20, and 30 wt.%) with metakaolin, while maintaining constant SiO_2/Al_2O_3 and Na_2O/Al_2O_3 molar ratios. The materials were prepared through alkali activation using sodium silicate and sodium hydroxide, followed by curing. Comprehensive characterization was carried out using X-ray fluorescence (XRF), X-ray diffraction (XRD), and scanning electron microscopy (SEM). In addition, adsorption experiments using methylene blue (MB) were conducted to evaluate the environmental performance of the synthesized geopolymers. The results revealed that the mine waste contains high concentrations of potentially toxic elements (up to 2.23 wt.% Pb and 8.2 wt.% Zn), highlighting the need for effective stabilization. Microstructural analysis confirmed the formation of predominantly amorphous geopolymer matrices with varying degrees of reaction depending on MW content. The highest compressive strengths (25–30 MPa) were achieved for formulations containing 5–10 wt.% MW after 28 days of curing. Furthermore, the geopolymers demonstrated efficient methylene blue removal, following pseudo-second-order kinetics and fitting the Langmuir isotherm model, with enhanced adsorption performance observed at higher MW contents. These findings indicate that MW-based geopolymers are promising materials for mine waste valorization and methylene blue removal. However, standardized leaching tests are required to confirm the long-term immobilization of Pb, Zn, Cd, As, and other potentially toxic elements within the geopolymer matrix. The study highlights their potential as sustainable, low-impact materials, supporting waste valorization and

Academic Editor: Michele John

Received: 19 April 2026
Revised: 25 May 2026
Accepted: 29 May 2026
Published: 15 June 2026

contributing to the development of environmentally resilient systems within a circular economy framework.

Keywords: mine waste; geopolymer; methylene blue; adsorption; compressive strength

1. Introduction

Mine waste MW, a by-product of mineral extraction processes, is typically considered as an environmental liability due to its significant volume and the potential to cause long-term environmental damage if not treated properly. The mining process produces huge amounts of tailings during the quarrying, milling, sorting, and processing of ores and minerals, which are typically discarded over large areas within the mine site, creating environmental concerns. For the extraction of one ton of metal, approximately 2–12 tons of overburden material are generated as waste rocks [1].

The mining industry is one of the largest waste producers globally, generating approximately 7 billion tons of tailings annually [2]. Recent projections suggest that by 2025, the total accumulation of solid tailings will reach 19 billion tons. This increase reflects the growing scale of mining operations and the corresponding rise in waste material generated. For instance, in the European Union alone, the stock of mine tailings has surpassed 1.5 billion tons [2]. This increase is attributed to the industry's shift towards mining lower-grade ores, which results in higher volumes of waste material per unit of extracted metal.

Recent findings around the world proved that mine wastes may contain harmful compounds, such as heavy metals and radioactive elements, which are hazardous for the environment and human health [3]. The effects of storage sites can result in accelerated erosion, sinkholes, loss of biodiversity, or the contamination of soil, groundwater, surface water and sea waters. These processes also affect the atmosphere through carbon emissions, which have an effect on the quality of human health and biodiversity.

In Tunisia, a country with a long mining heritage history, it has been proven that mine discharges are a source of metal accumulation in plants [4,5], soils [6,7], marine environments [8,9], and water and stream sediments [10,11]. Additionally, the studies of Srarfi et al. [12] and Ayari et al. [13] showed that mine waste is at the origin of degradation and abnormal metal contents found in stream sediments. These findings highlight the threat of mine discharge to surface water supplies in Tunisia, since results showed that metals from mine waste may be responsible for the potentially hazardous level of nutriments in ground water [10].

The old mine of Lakhouat located in the northwest of Tunisia has been the subject of many studies [3,5,14,15]. Like the majority of Pb-Zn mines located in the Medjerda basin, the most important supplier of freshwater for the entire country, the site was at the origin of bulky abandoned residues, which are highly subject to erosion. Metal recovery through the extraction method was only partial, leaving significant residual metals unextracted [15]. Consequently, these potentially toxic element (PTE)-rich dumps are likely to pollute large areas around the old mine, starting with topsoil and vegetation [3,16].

Recent environmental initiatives and research findings focus on minimizing waste production, resulting in savings in raw materials and disposal costs and, most importantly, in potential reduction of environmental impact of MW [17]. However, recent studies have shown that mine waste can be transformed into geopolymers through a process known as geopolymerization. This approach presents a unique opportunity to simultaneously address the challenges associated with mine waste disposal while producing eco-friendly

construction materials. In addition, geopolymer matrices have been investigated for the immobilization of potentially toxic elements in contaminated materials, including As, Cr, Mo, Pb, Sb, Se, and Zn [18].

One of the primary advantages of geopolymers derived from mine wastes is their enhanced mechanical performance. Geopolymers exhibit excellent compressive and flexural strengths comparable to or even surpassing those of traditional cement-based materials [19–21]. This high strength makes geopolymers suitable for a wide range of applications, including structural elements and infrastructure components. Furthermore, the increased durability and resistance to chemical attacks demonstrated by geopolymers can extend the lifespan of constructed assets, thereby reducing maintenance and replacement costs [22]. Also, it has been shown that the use of geopolymer based materials for coastal infrastructures projects, such as seawalls, breakwaters and harbor structures, can offer superior durability and resistance to saltwater corrosion compared to Portland cements [23].

In addition to their mechanical properties, geopolymers offer significant environmental benefits. Geopolymer production emits significantly lower levels of carbon dioxide compared to cement manufacturing [24–26], resulting in a reduced carbon footprint. This reduction in CO_2 emissions aligns with global efforts to mitigate climate change and promotes sustainable practices in the construction sector.

On the other hand, the utilization of geopolymers as adsorbents for dyes is a significant advancement in the field of material engineering [27]. The importance of this application lies in its potential to address two pressing global challenges simultaneously: environmental pollution and sustainable materials development. Geopolymer technology, with its unique properties, offers an eco-friendly solution for a wide range of harmful synthetic dyes from waste waters [28,29], potentially contributing to the preservation of ecosystems and water resources. Considering the detrimental environmental and health impacts of nondegradable synthetic dyes, as highlighted by Khan and Malik [30], their contamination of water resources poses a dual threat. Not only do these dyes pollute water but their toxic nature also poses risks to human health. Moreover, their presence in aquatic systems, even at low concentrations, has been found to impede photosynthesis due to a reduction in light penetration [31]. Consequently, the discernible and undesirable effect of trace amounts of these micropollutants (<1 ppm) in industrial wastewater has been well-established [32]. Methylene blue (MB), a dye commonly utilized in the fabrics and furniture industries, exemplifies the severity of the issue. The occurrence of MB in effluent water has been associated with severe health consequences, including permanent blindness, asthma, and abdominal disorders such as vomiting and nausea [33,34]. Given the evident risks to both human health and the environment, the imperative to remove MB from water effluents becomes increasingly apparent.

This study explores the valorization of Pb–Zn mine waste in metakaolin-based geopolymers within a circular economy framework. The utilization of mine waste in geopolymer synthesis contributes to waste reduction, resource efficiency, and the creation of value-added materials from an environmental liability. In this work, the intended application is considered multifunctional but differentiated according to the tested material form. The geopolymer bodies were evaluated as bulk materials through compressive strength, SEM/EDS, and micro-CT analyses, providing information relevant to construction-related applications, including potential use in coastal or marine contexts. In contrast, methylene blue adsorption was assessed using milled geopolymer powder as a preliminary screening of water treatment potential. Therefore, the findings of this study address the challenges of mine waste management while supporting circular economy principles by combining waste reuse, sustainable material development, and preliminary assessment of dye removal functionality.

2. Results and Discussion

2.1. Material Characterization

2.1.1. Particle Size Distribution

Figure 1 illustrates the particle size distribution of mine waste (MW) obtained in the laboratory and metakaolin (VPMK). The particle size distribution of MW demonstrates a bimodal nature, with a dominant population of particles between 10 and 100 µm, and a secondary population in the finer range, between 0.4 and 60 µm, resulting in an average particle size of approximately 15 µm. This bimodal distribution indicates the presence of two distinct particle size populations, which may be attributed to variations in the crushing and milling processes or the natural heterogeneity of the source material.

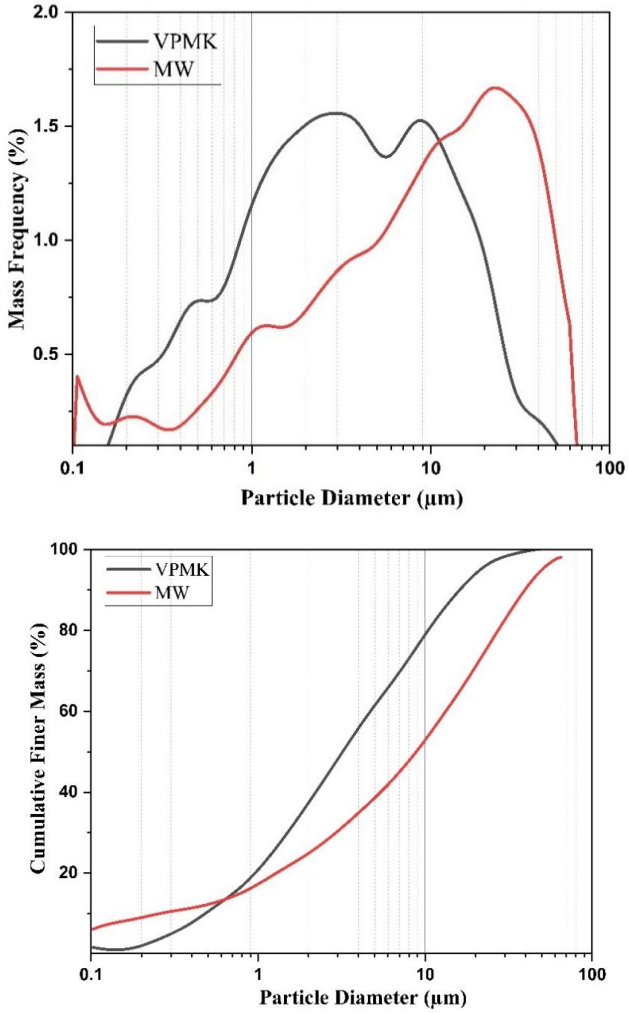

Figure 1. Particle size distribution of MW and VPMK materials.

In contrast, the particle size distribution of VPMK is unimodal, with a narrow range of particle sizes predominantly falling between 1 and 10 µm and a mean size of approximately 6 µm. The unimodal distribution of VPMK suggests that the material has undergone more controlled processing, resulting in a finer and more uniform particle size compared to MW.

The comparison of these materials highlights the difference in particle size characteristics, where MW, with its broader and bimodal distribution, consists of a mixture of coarse and fine particles, whereas VPMK is composed primarily of finer particles with a more uniform distribution.

2.1.2. Mineralogical Analysis

The XRD patterns of the MW and VPMK are both presented in Figure 2. The sampling strategy adopted in this work is consistent with previous investigations [3] conducted on the same mine waste deposit, the characteristics of which have been discussed in detail.

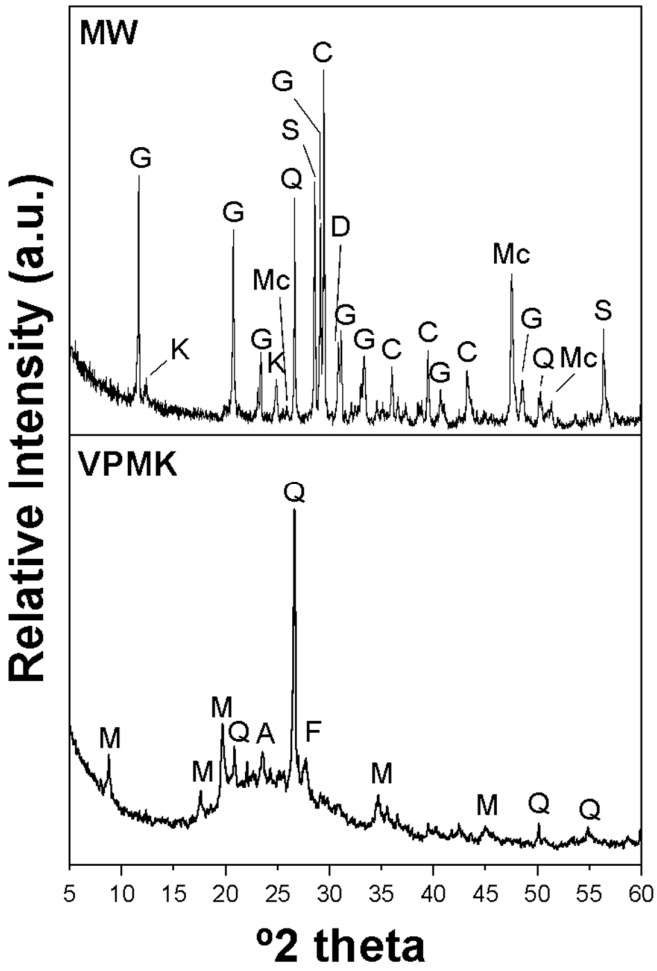

Figure 2. XRD patterns of materials. MW, mine waste; VPMK, Vicente Pereira metakaolin; A, anatase; C, calcite; D, dolomite; F, feldspar; G, gypsum; K, kaolinite; M, muscovite; Mc, marcasite; Q, quartz; S, sphalerite.

The XRD pattern of the MW reveals a mineral composition characteristic of a carbonated geological context. The dominant presence of calcite and dolomite reflects the prevalence of carbonate minerals in the region, which is typical for mining environments in northern Tunisia [35]. This carbonated context is reinforced by the significant detection of quartz indicating that silicate-rich phases coexist with the carbonates. The presence of gypsum points to secondary mineralization processes, potentially arising from the interaction of sulfides and the carbonate-rich host rocks. The presence of kaolinite further indicates the occurrence of aluminosilicate phases in the MW. The detection of sphalerite and marcasite confirms the presence of Pb-Zn sulfide minerals, which are typical of ore deposits in northern Tunisia. These sulfides, when exposed to atmospheric conditions, may lead to environmental concerns such as acid mine drainage, particularly in a region with carbonate-rich geology.

The XRD pattern of VPMK is characteristic of calcined kaolin/metakaolin, with a broad amorphous aluminosilicate band between approximately 15 and 32° 2θ, centered near 24° 2θ. This amorphous contribution is related to the dehydroxylation of kaolinite during calcination at 700 °C for 4 h, resulting in the formation of reactive metakaolin

suitable for geopolymerization [36]. The main crystalline phase observed in VPMK is quartz, together with minor accessory phases, such as muscovite, anatase, and feldspar, inherited from the original kaolin raw material. The presence of anatase is common in natural kaolin deposits and is useful for characterizing the source material, although it does not contribute significantly to pozzolanic/geopolymeric reactivity [37]. No residual kaolinite reflections were identified in the VPMK pattern.

The SEM image of MW (Figure 3) reveals the complex morphology of the particles, highlighting a wide range of sizes and shapes. The image shows a mixture of angular and irregularly shaped particles, which is consistent with the material's mechanical processing during mining and crushing. The angular nature of the particles suggests limited weathering or erosion, which typically results in more rounded particles.

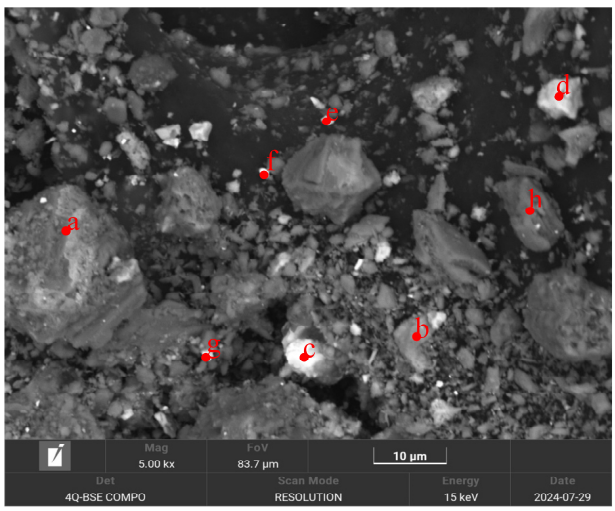

a

Element	Atomic %	Weight %
Aluminum	0.82	0.85
Cadmium	0.36	1.58
Calcium	32.31	50.29
Carbon	12.74	5.94
Iron	1.80	3.91
Lead	0.17	1.35
Oxygen	46.85	29.11
Silicon	1.16	1.26
Sulphur	3.04	3.78
Zinc	0.75	1.91

b

Element	Atomic %	Weight %
Aluminum	0.50	0.77
Calcium	7.41	17.15
Carbon	37.02	25.68
Oxygen	52.45	48.47
Silicon	0.58	0.94
Sulphur	0.39	0.71
Zinc	1.66	6.27

c

Element	Atomic %	Weight %
Aluminum	1.57	0.84
Barium	3.95	10.76
Cadmium	1.56	3.48
Calcium	15.89	12.63
Carbon	6.81	1.62
Copper	11.55	14.56
Iron	8.72	9.66
Lead	5.67	23.30
Oxygen	34.63	10.99
Silicon	3.66	2.04
Thallium	0.84	3.41
Zinc	5.16	6.70

d

Element	Atomic %	Weight %
Carbon	51.72	22.44
Lead	0.66	4.94
Oxygen	10.66	6.16
Potassium	0.27	0.38
Strontium	0.32	1.02
Sulphur	17.33	20.07
Zinc	19.04	44.98

e

Element	Atomic %	Weight %
Aluminum	0.44	0.28
Barium	3.78	12.19
Calcium	6.74	6.33
Carbon	43.28	12.19
Lead	9.06	44.01
Oxygen	21.24	7.97
Rubidium	0.29	0.59
Sulphur	13.74	10.33
Tungsten	1.42	6.11
Zinc	0.01	0.01

f

Element	Atomic %	Weight %
Aluminum	1.34	1.37
Calcium	1.04	1.58
Carbon	46.60	21.25
Lead	5.09	40.01
Oxygen	43.18	26.22
Strontium	0.81	2.69
Tungsten	0.45	3.16
Zinc	1.49	3.70

g

Element	Atomic %	Weight %
Aluminum	2.14	1.01
Barium	4.35	10.50
Cadmium	1.37	2.71
Calcium	6.81	4.79
Carbon	0.05	0.01
Copper	13.11	14.63
Iron	8.68	8.51
Lead	10.73	39.05
Oxygen	45.17	12.69
Silicon	4.13	2.04
Strontium	0.22	0.35
Zinc	3.23	3.71

h

Element	Atomic %	Weight %
Aluminum	0.53	0.53
Barium	0.33	1.70
Cadmium	0.41	1.70
Calcium	24.45	36.36
Carbon	27.40	12.21
Lead	0.74	5.71
Oxygen	23.38	13.88
Silicon	0.85	0.89
Strontium	0.08	0.25
Sulphur	21.18	25.20
Zinc	0.65	1.57

Figure 3. SEM images of the mine waste.

In terms of particle size, the SEM image confirms the heterogeneity of the MW, with coarse particles appearing alongside finer material. The presence of both large and small particles aligns with the previously identified bimodal particle size distribution, which shows dominant populations of coarse particles above 10 µm and finer particles below this size.

The mineralogical analysis of a representative sample of MW is presented in Figure 2 and reveals distinct gangue and metallic element compositions.

SEM analysis confirmed the presence of calcite ($CaCO_3$) (Figure 3a,b) as a host rock mineral, highlighting the carbonate-rich nature of the host rock. Based on the elemental composition (Figure 3b), the presence of sulfur (0.71%) and zinc (6.27%) suggests the possible inclusion of minor sulfate or zinc oxide/sulfide compounds.

The metallic elements originate from the primary sulfide ores, including galena (PbS) (Figure 3c) and sphalerite (ZnS) (Figure 3d), which undergo oxidation upon exposure to atmospheric conditions, leading to the formation of secondary minerals like anglesite ($PbSO_4$) (Figure 3e), cerussite ($PbCO_3$) (Figure 3f), and barite ($BaSO_4$) (Figure 3g). The interaction of sulfuric acid with galena produces anglesite, while carbonate ions from the host rock facilitate the formation of cerussite. The oxidation of pyrite (FeS_2) further drives the formation of sulfate-based minerals. Gypsum ($CaSO_4 \cdot 2H_2O$) (Figure 3h) is classified as a secondary mineral, formed through the interaction of calcium with sulfuric acid produced by the oxidation of sulfide minerals. This mineral assemblage highlights the role of sulfide oxidation and the carbonated environment in shaping the geochemical processes and secondary mineralization in MW.

2.1.3. Waste Chemical Analysis

Chemical analysis of the MW (Table 1) shows that the major element is SO_3 (24.61 wt.%), attributed to the presence of gypsum, also detected in XRD and SEM. High amounts of iron and zinc (8.7 wt.% and 8.2 wt.%, respectively), reported in Table 2, correspond to the presence of marcasite (FeS_2) and sphalerite (ZnS), respectively. These findings suggest potential environmental concerns due to the high sulfur content and the possibility of acidic leaching. CaO is the second-most abundant oxide (22.68 wt.%), originating from carbonate gangue. Al_2O_3 (4.6 wt.%) and SiO_2 (10.9 wt.%) corroborate the presence of kaolinite, and the latter of quartz also in the MW XRD pattern (Figure 2). MgO (~1 wt.%) is associated with dolomite admixture in MW.

Table 1. Chemical analysis of materials.

	Composition (wt.%)									
	SO_3	**MgO**	**Al_2O_3**	**SiO_2**	**P_2O_5**	**K_2O**	**CaO**	**TiO_2**	**Fe_2O_3**	**L.O.I.**
MW	24.61	0.92	4.60	10.91	0.09	0.18	22.68	0.23	8.69	14.73
VPMK	0.02	0.32	39.88	52.05	0.06	1.28	0.12	1.55	2.17	2.31

L.O.I., loss on ignition.

Table 2. Concentration of potentially toxic elements (PTEs) in the MW.

	Composition							
	Pb (wt.%)	**Zn (wt.%)**	**Sr (ppm)**	**Ba (ppm)**	**Cd (ppm)**	**Ni (ppm)**	**Cr (ppm)**	**As (ppm)**
MW	2.23	8.2	4740	8210	3860	160	97.3	200

The lead (2.23 wt.%) and zinc (8.2 wt.%) concentrations are consistent with the presence of Pb-Zn sulfide minerals such as galena (PbS) and sphalerite (ZnS), also identified through XRD and SEM. Additionally, the presence of Ba (8210 ppm) and Sr (4740 ppm) points to barite ($BaSO_4$) and strontium-rich minerals, which are often associated with lead–zinc mining environments. The PTEs (potentially toxic elements) like Cd, As, Ni, and Cr further highlight the environmental risks posed by the waste, as these elements are commonly linked to mine tailings and their potential leaching into the environment.

These very high values, surpassing typical background values [3], are due to the nature of the ore and the inability of the industrial process to recover all the metals. High

PTE concentrations in MW were previously reported near several mining sites in Tunisia and other countries with comparative situations worldwide [38–40].

Further research showed that these alarming values present a real threat to the environment (plants, soils, water) and human health [3,14]. Therefore, finding a way to successfully reuse these waste sources is a great step towards circular economy and sustainability.

The chemical composition of the VPMK, shown in Table 1, is characterized by significant amounts of silicon dioxide (SiO_2) and aluminum oxide (Al_2O_3), constituting 52.05 wt.% and 39.88 wt.%, respectively. This high content of reactive silica and alumina is crucial for the geopolymerization process, as they interact under alkaline conditions to form the aluminosilicate gel that provides the structural framework of the geopolymer [41]. Fe_2O_3 (2.17 wt.%) indicates the presence of iron oxides/oxyhydroxides in the MK sample; this is due to a low crystallinity not detected by XRD analysis. Additionally, K_2O (1.28 wt.%) is ascribed to alkali feldspar and muscovite and TiO_2 (1.55 wt.%) to anatase, all detected in the VPMK XRD pattern (Figure 2). The presence of metakaolin in the VPMK sample is confirmed by a characteristic amorphous band between 15–32° (2θ) with its center at 24° (2θ). The high loss on ignition (L.O.I., 2.31%) reflects the dehydroxylation of kaolinite during the calcination process that converts kaolin into metakaolin. This enhances its reactivity, making it ideal for use in sustainable building materials.

2.2. Geopolymer Specimen Characterization

2.2.1. X-Ray Diffraction Analysis (XRD)

Mineralogical composition of the geopolymers at 1 and 28 days of curing are presented in Figure 4. No significant changes in XRD patterns of individual geopolymers at 1 and 28 curing days are observed. However, it is noticeable that XRD patterns of individual geopolymer formulations differ in the presence of an amorphous phase and crystallinity. The XRD pattern of VPMK100 is characterized by a broad band related to amorphous silico-aluminate framework, resulting from the activation of metakaolin by alkaline activators. Compared to the XRD pattern of metakaolin (Figure 2), there is a shift in the amorphous reflection to a center of ~28°2 theta, which is characteristic of the changes in the structure of metakaolin during geopolymerization. Moreover, diffractions of unreacted admixtures, such as quartz, muscovite, and anatase, are still present in VPMK100. The amorphous nature of geopolymers decreases with an increased amount of MW in the composition. Crystalline phases of MW (quartz, marcasite, calcite, and sphalerite) dominate in XRD patterns of VPMK95 to VPMK70, whereas intensities of admixtures belonging to metakaolin (muscovite, anatase, and feldspar) became suppressed (Figure 2). This suggests that under the conditions tested, MW acted mainly as a mineral filler/additive within the geopolymer matrix, whereas metakaolin remained the principal reactive aluminosilicate precursor responsible for geopolymer gel formation. Moreover, reflections of gypsum in all geopolymers with MW disappeared, indicating that gypsum became a part of amorphous matrix.

2.2.2. Scanning Electron Microscope (SEM/EDS) Analysis

Figures 5–7 present SEM images representative of geopolymers VPMK100, VPMK90, and VPMK70 and performed after 28 days of curing.

The SEM analysis of a geopolymer synthesized with 100% metakaolin reveals a uniform and homogeneous morphology (Figure 5) with a characteristic gel network typical of metakaolin-based geopolymers [42]. The image typically displays a compact surface indicative of the consistent aluminosilicate matrix formed during the geopolymerization process. The absence of heterogeneous materials contributes to the uniform texture, with minimal porosity and no visible inclusions or coarse particles. The occurrence of Si, Al,

Na, and O simultaneously in the SEM image reflects the chemical composition of the aluminosilicate gel and the contribution of the sodium activator in the formation of the geopolymer matrix and the hardening of the geopolymer paste [43]. These elements are integral to the structural integrity and chemical stability of the geopolymer.

The addition of 30% MW to the geopolymer significantly alters the matrix, resulting in a more heterogeneous microstructure, as observed through SEM analysis in Figure 6A. This heterogeneity is due to the diverse composition of the MW, which introduces various mineral phases, oxides, and metallic elements that disrupt the otherwise uniform aluminosilicate gel network formed by the geopolymerization process. The SEM images typically show unreacted or partially reacted particles, irregular pore structures, and inclusions of MW materials. This heterogeneous structure highlights the interaction between the metakaolin and the MW, resulting in a more complex and less uniform geopolymer matrix.

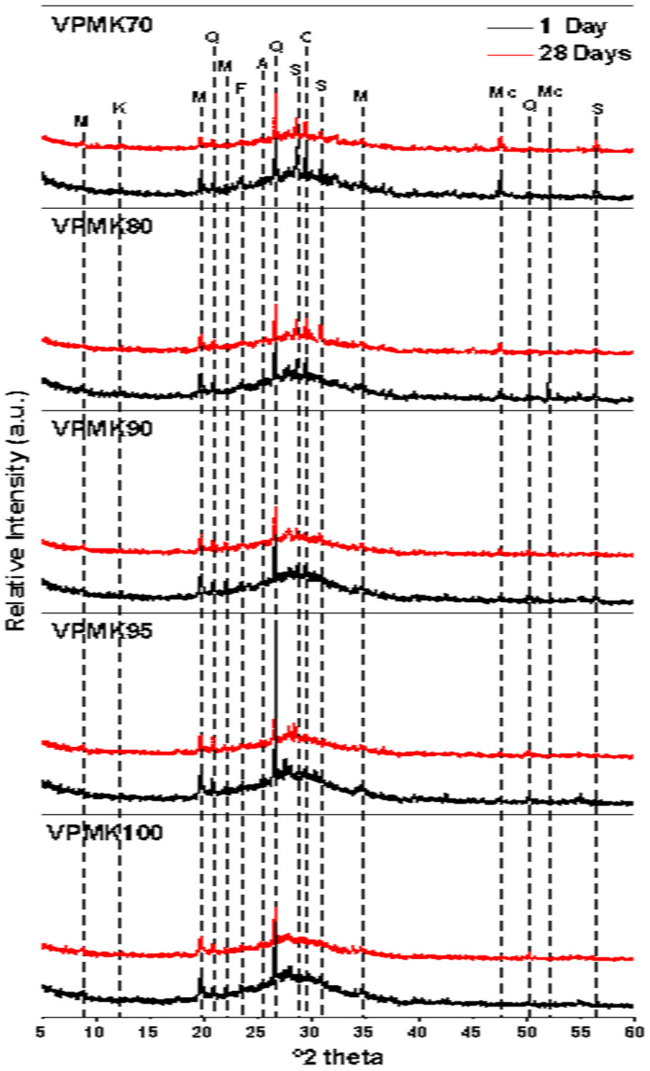

Figure 4. XRD patterns of the geopolymers (A, anatase; C, calcite; F, feldspar; K, kaolinite; M, muscovite; Mc, marcasite; Q, quartz; S, sphalerite).

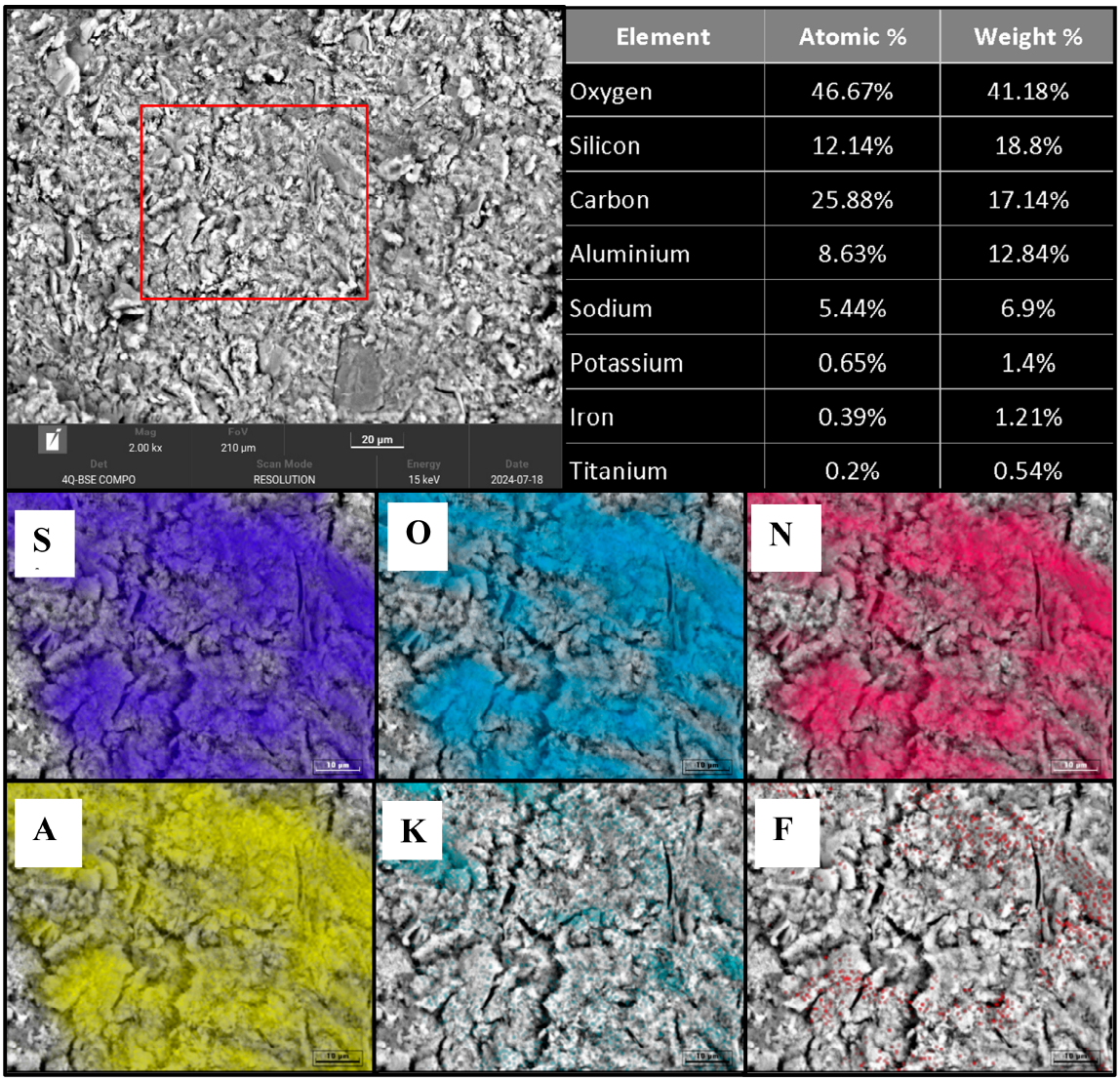

Element	Atomic %	Weight %
Oxygen	46.67%	41.18%
Silicon	12.14%	18.8%
Carbon	25.88%	17.14%
Aluminium	8.63%	12.84%
Sodium	5.44%	6.9%
Potassium	0.65%	1.4%
Iron	0.39%	1.21%
Titanium	0.2%	0.54%

Figure 5. SEM/EDS micrographs of VPMK100 geopolymer at 28 days of curing.

Figure 6B reveals a pore structure that is partially filled with mineral deposits originating from the MW. Close inspection through EDS analysis shows the presence of sphalerite, indicating that minerals from the MW have infiltrated and precipitated within the void spaces of the geopolymer matrix. The presence of sphalerite in the pore suggests that the MW not only contributes to the heterogeneous nature of the geopolymer but also plays a role in filling and reinforcing the pore structure, potentially improving the material's mechanical properties. This interaction between the pore spaces and MW minerals reflects the complex integration of waste materials within the geopolymer framework.

Figure 6C reveals a Ca-Si-Al phase at point P1, with a composition (Si = 19.87 wt.%, Al = 10.08 wt.%, Ca = 1.24 wt.%, Na = 15.71 wt.%) consistent with the possible formation of a calcium aluminosilicate hydrate (C-A-S-H) region alongside the N-A-S-H gel matrix. Under the alkaline activation conditions of this study, Ca^{2+} ions released from gypsum and calcite dissolution may interact with silicate and aluminate species to promote C-A-S-H formation as reported for calcium-rich geopolymer systems [44,45]. This interpretation remains, however, a working hypothesis, as direct confirmation would require ^{29}Si MAS-NMR or FTIR analyses. The incorporation of calcium can result in denser gel networks but it also risks forming unwanted crystalline phases if the balance of reactants is not

ideal, potentially affecting material properties [46,47]; this result will be further discussed subsequently.

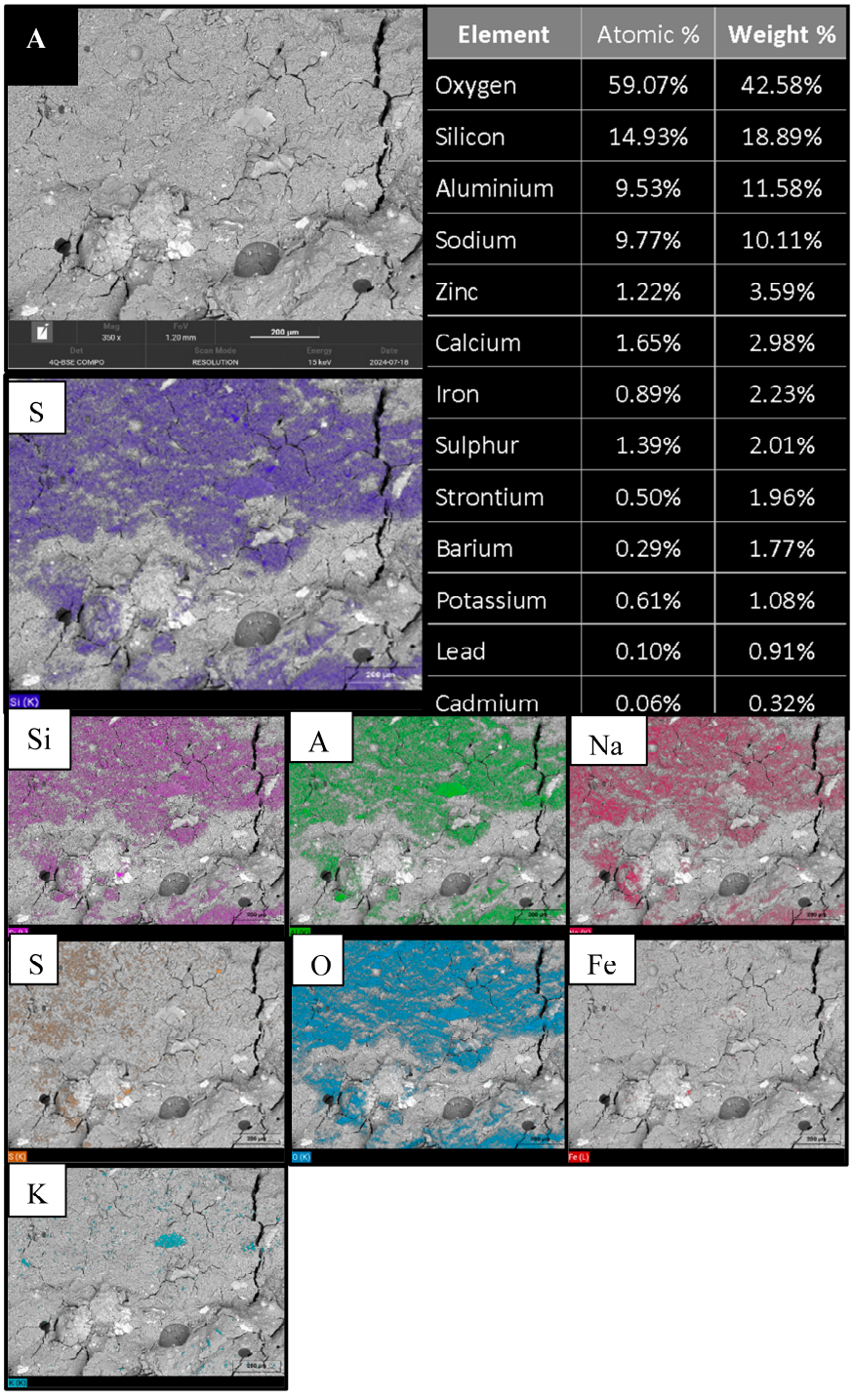

Element	Atomic %	Weight %
Oxygen	59.07%	42.58%
Silicon	14.93%	18.89%
Aluminium	9.53%	11.58%
Sodium	9.77%	10.11%
Zinc	1.22%	3.59%
Calcium	1.65%	2.98%
Iron	0.89%	2.23%
Sulphur	1.39%	2.01%
Strontium	0.50%	1.96%
Barium	0.29%	1.77%
Potassium	0.61%	1.08%
Lead	0.10%	0.91%
Cadmium	0.06%	0.32%

Figure 6. *Cont.*

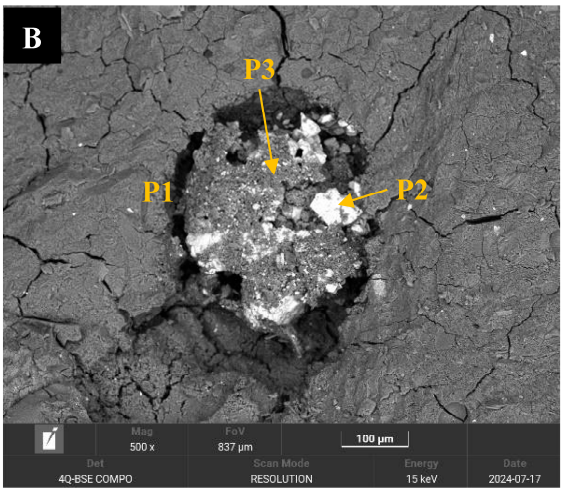

P2 Element	Atomic %	Weight %
Zinc	40.97%	61.27%
Sulphur	45.1%	33.07%
Oxygen	11.89%	4.35%
Silicon	2.04%	1.31%

P3 Element	Atomic %	Weight %
Oxygen	56.95%	38.66%
Silicon	19.8%	23.6%
Aluminum	10.85%	12.42%
Zinc	3.02%	8.38%
Iron	2.58%	6.12%
Calcium	3.01%	5.13%
Sulphur	2.32%	3.15%
Titanium	1.04%	2.12%
Sodium	0.42%	0.41%

P1 Element	Atomic %	Weight %
Oxygen	60.88%	47.58%
Silicon	14.48%	19.87%
Sodium	13.99%	15.71%
Aluminum	7.65%	10.08%
Sulphur	1.7%	2.67%
Zinc	0.55%	1.76%
Calcium	0.63%	1.24%
Lead	0.11%	1.1%

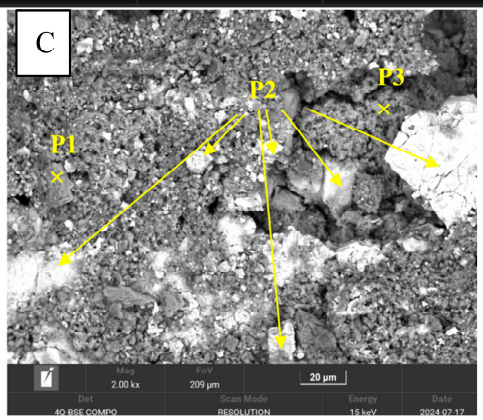

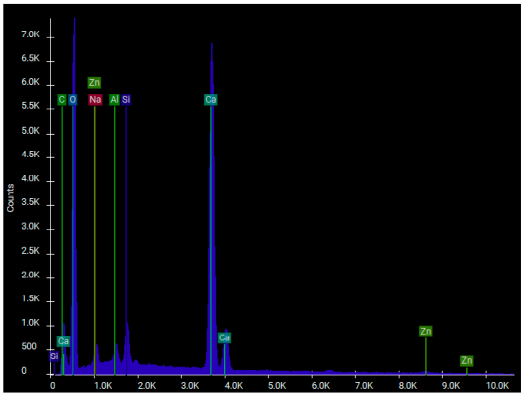

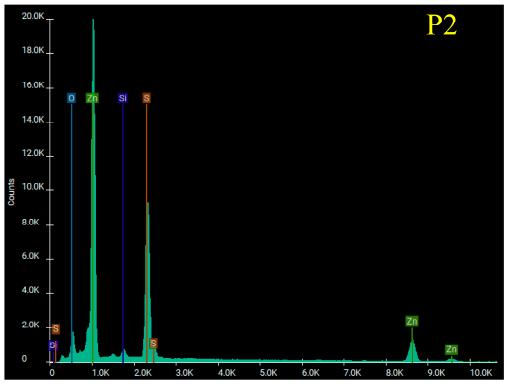

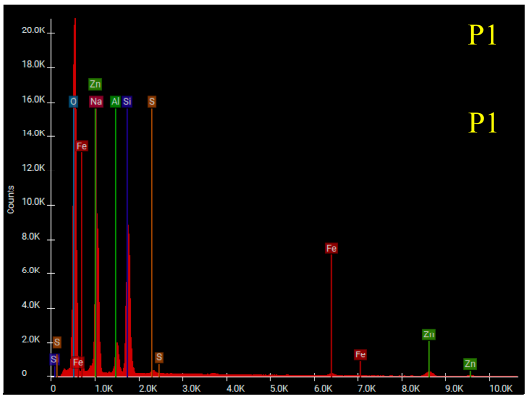

Figure 6. *Cont.*

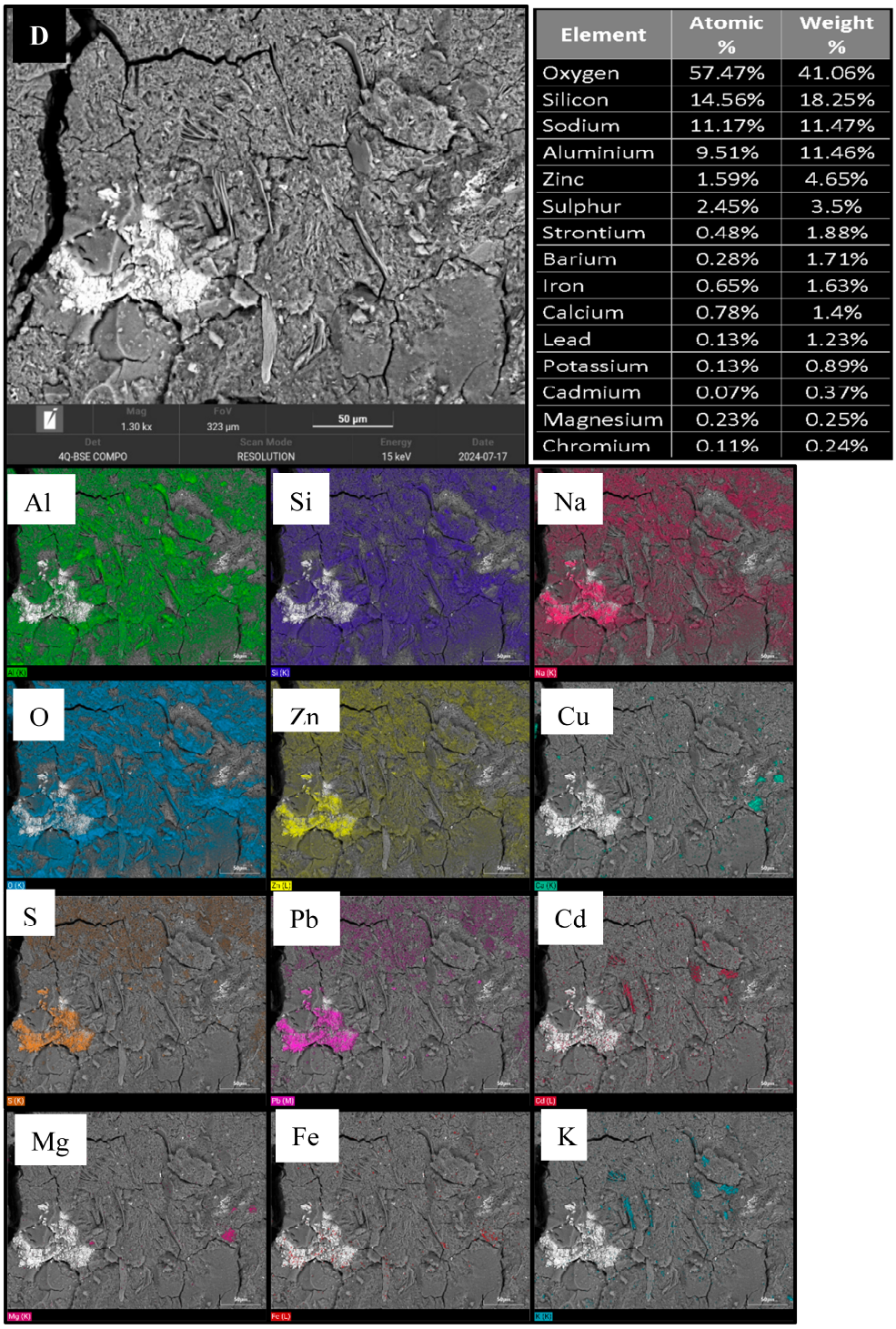

Element	Atomic %	Weight %
Oxygen	57.47%	41.06%
Silicon	14.56%	18.25%
Sodium	11.17%	11.47%
Aluminium	9.51%	11.46%
Zinc	1.59%	4.65%
Sulphur	2.45%	3.5%
Strontium	0.48%	1.88%
Barium	0.28%	1.71%
Iron	0.65%	1.63%
Calcium	0.78%	1.4%
Lead	0.13%	1.23%
Potassium	0.13%	0.89%
Cadmium	0.07%	0.37%
Magnesium	0.23%	0.25%
Chromium	0.11%	0.24%

Figure 6. SEM/EDS micrographs of VPMK70 geopolymer at 28 days of curing. (**A**) SEM/EDS characterization of the VPMK70 geopolymer matrix; (**B**) SEM micrograph showing the analysed region with selected points; (**C**) SEM micrograph and EDS spectra of selected regions in VPMK70 geopolymer; (**D**) SEM micrograph showing the morphology of the geopolymer matrix.

Figure 6C also reveals the presence of numerous ZnS (Sphalerite) particles, P2, attributed to the MW incorporated into the geopolymer matrix. These ZnS particles, derived from zinc-containing minerals in the waste, are distributed throughout the matrix. Their presence indicates an interaction between the MW and the geopolymer structure, potentially affecting the material's microstructure and durability.

The fibrous particles observed in Figure 6D may be associated with C-S-H or C-A-S-H phases, a morphology commonly reported in calcium-containing geopolymer systems [48,49]. However, direct identification of these phases was not achieved in the present study, and further mineralogical and microstructural investigations are recommended in future work to confirm their nature and role within the geopolymer matrix.

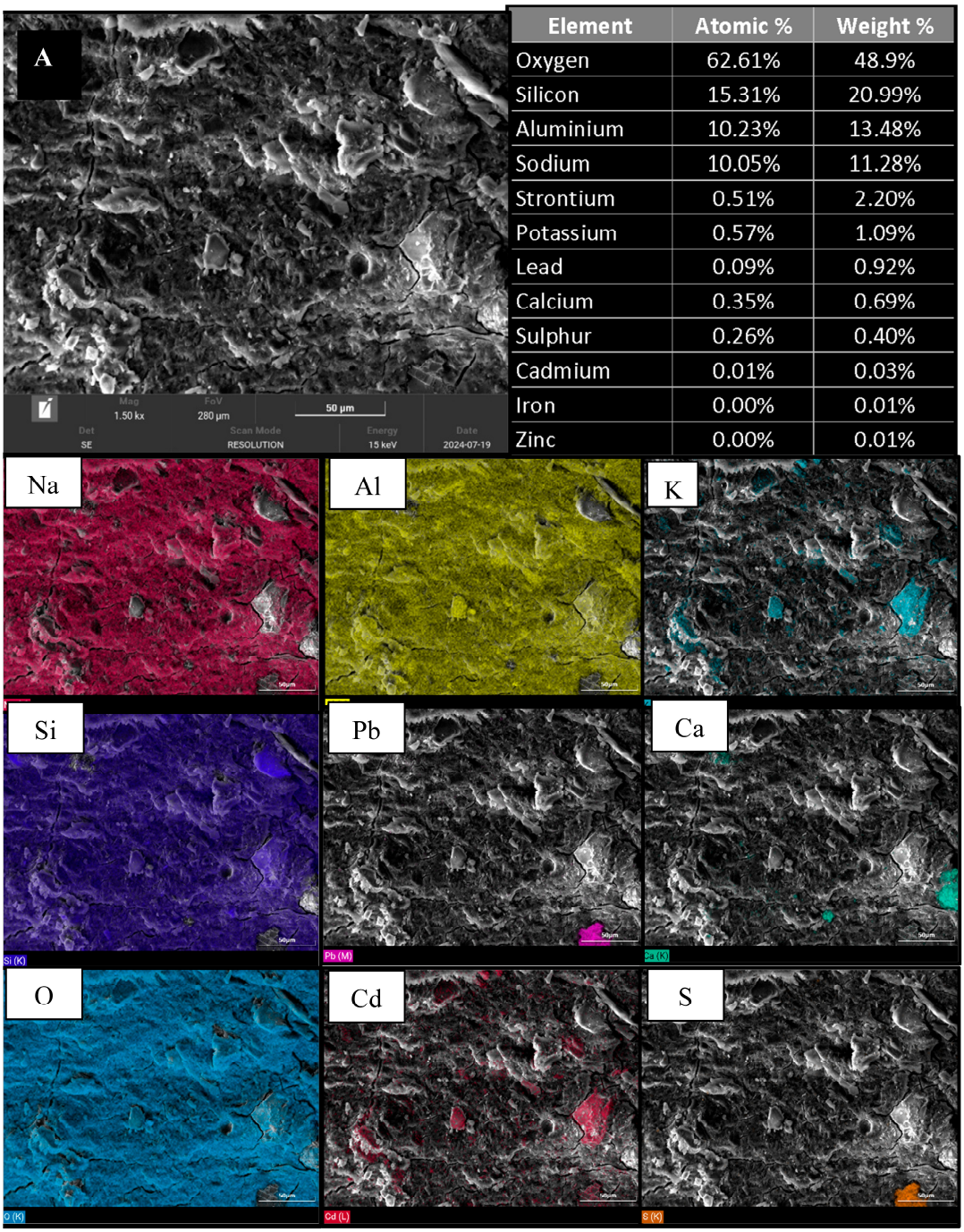

Figure 7. *Cont.*

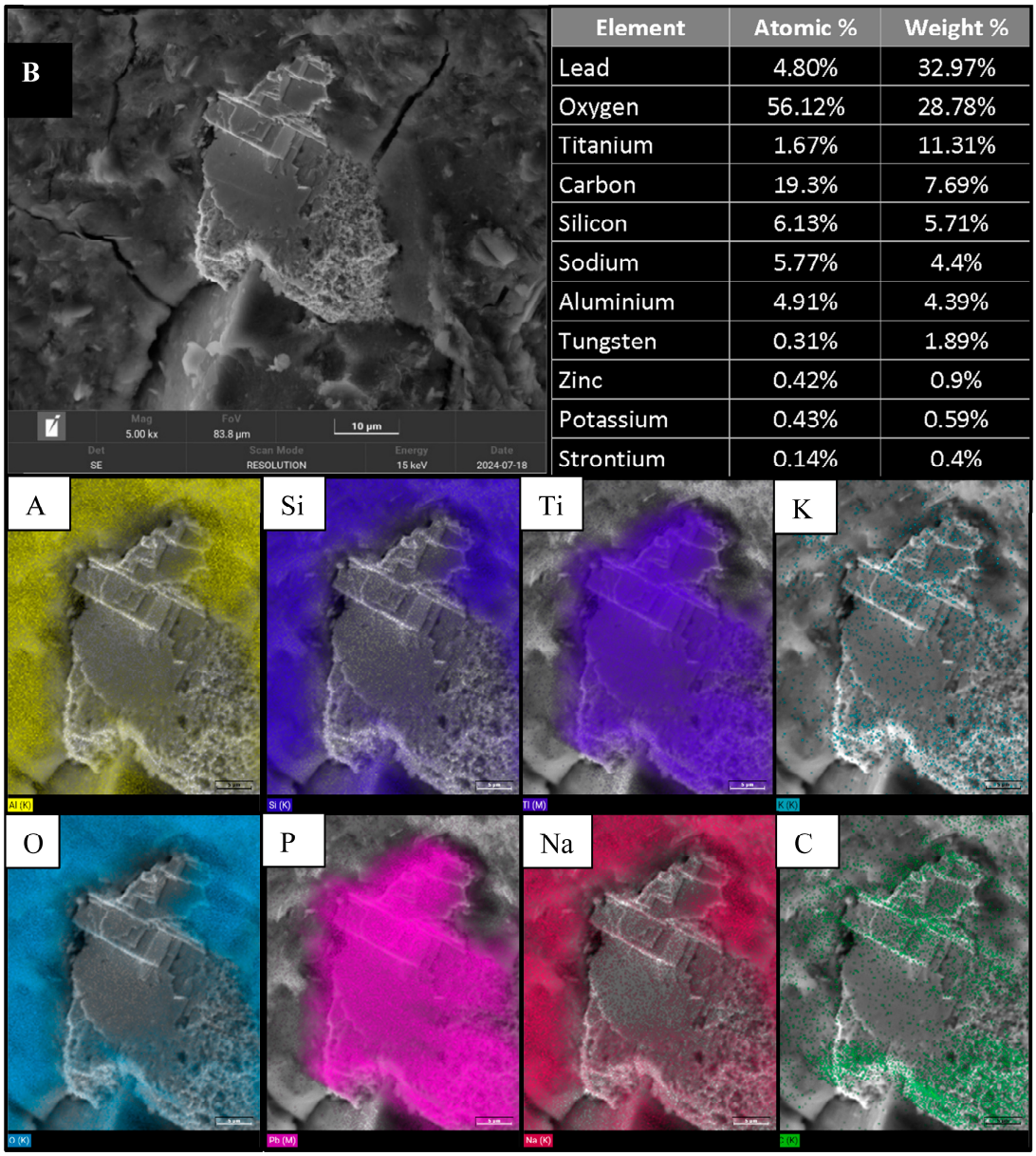

Element	Atomic %	Weight %
Lead	4.80%	32.97%
Oxygen	56.12%	28.78%
Titanium	1.67%	11.31%
Carbon	19.3%	7.69%
Silicon	6.13%	5.71%
Sodium	5.77%	4.4%
Aluminium	4.91%	4.39%
Tungsten	0.31%	1.89%
Zinc	0.42%	0.9%
Potassium	0.43%	0.59%
Strontium	0.14%	0.4%

Figure 7. SEM/EDS micrographs of VPMK90 geopolymer at 28 days of curing. (**A**) SEM micrograph of the geopolymer matrix; (**B**) SEM micrograph of a lead-rich particle embedded in the geopolymer matrix.

Figure 7 displays SEM images of the geopolymer samples incorporating 10% MW after a 28-day curing period. The images reveal a heterogenous but compact morphology, indicating that the geopolymer matrix has a varied structure with areas of different compositions and structures due to the inclusion of the MW. However, despite this variety, the material is dense and well bonded overall. This compactness suggests good cohesion within the matrix, which is crucial for mechanical strength. The heterogeneity reflects the diverse mineral phases (Figure 7A) induced by the MW which interact with the geopolymer matrix during curing. Additionally, the presence of galena PbS (Figure 7B) particle, originating from the MW, is visible within the matrix, indicating successful incorporation of the MW minerals into the geopolymer structure.

Although SEM/EDS observations show that ZnS- and PbS-bearing particles are incorporated within the geopolymer matrix, this evidence alone does not confirm their long-term chemical stability. Sphalerite (ZnS) and galena (PbS) are generally low-solubility sulfide

phases under neutral to alkaline conditions, and their physical encapsulation within the geopolymer matrix may reduce direct exposure to external solutions. However, the dissolution and surface alteration of sphalerite are pH-dependent, and galena can undergo oxidative dissolution, releasing aqueous Pb and sulfate and forming secondary Pb-bearing phases, such as anglesite or cerussite, under different environmental conditions [50,51]. Therefore, ZnS- and PbS-bearing particles can be considered relatively stable within the alkaline geopolymer matrix, but they may still represent a potential long-term leaching risk if matrix degradation, carbonation, cracking, oxidation, or prolonged water ingress occurs. This aspect should be further evaluated in future studies through standardized leaching and durability tests.

2.2.3. Tomography

The tomography images of various geopolymer samples (Figure 8), ranging from VPMK100 to VPMK70, provide a clear visualization of particle distribution and integration within the geopolymer matrix. The analysis highlights the distribution of heavier MW particles (depicted as lighter in the tomography images), showing a consistent and homogeneous spread throughout the samples.

In VPMK100, which contains no MW, the light particles are likely quartz, a primary component of metakaolin. This uniform distribution underscores the refined nature of metakaolin as a reliable binder for geopolymer production. As the percentage of MW increases in VPMK95, VPMK90, VPMK80, and VPMK70, the tomography shows a corresponding increase in the presence of lighter MW particles. Despite the increasing quantity of MW, the particle distribution remains homogenous across the x, y, and z planes. This uniform dispersion is crucial for ensuring the mechanical properties and structural integrity of the geopolymer material.

The cross-sectional views further demonstrate that the blending process successfully integrates MW into the geopolymer matrix, providing a uniform structure across all axes. Such uniformity is vital for maintaining the functional properties of the geopolymer, especially in terms of strength and durability, which are key to its applications in construction.

In line with similar studies such as that by Chung et al. [52], the tomography method effectively visualizes the microstructural characteristics of geopolymers, offering insights into the distribution and behavior of particles within composite materials. This method is instrumental in optimizing the performance of geopolymers, particularly when incorporating industrial by-products like MW into sustainable construction materials.

2.2.4. Compressive Strength

Figure 9 illustrates the compressive strengths of geopolymers after curing periods of 1, 14, and 28 days. In general, there is an increase in compressive strength values from 1 to 14 days for geopolymers; this is more evident in geopolymers with MW incorporation. The values are presented as mean compressive strength values obtained from triplicate measurements, and the error bars represent the corresponding standard deviations. The data reveal a slight increase in compressive strength for VPMK100—from 19.23 MPa after a single day of curing to 20.5 MPa over 28 days.

The incorporation of MW into the geopolymer mixture resulted in the VPMK90 sample achieving a compressive strength of 29.5 MPa after 28 days of curing, surpassing that of the VPMK100 sample without MW. However, when the MW content in the mixture exceeded 10%, a decline in compressive strength was observed (17.69 MPa for VPMK80 and 11.24 MPa for VPMK70). The compressive strength values are presented as mean values obtained from triplicate measurements, with error bars representing the corresponding standard deviations. The standard deviations indicate acceptable reproducibility and

support the overall trend observed among the formulations, particularly the higher mean strength of VPMK90 after 28 days. However, because only triplicate measurements were performed, the results are discussed in terms of observed trends and reproducibility rather than as a full statistical optimization.

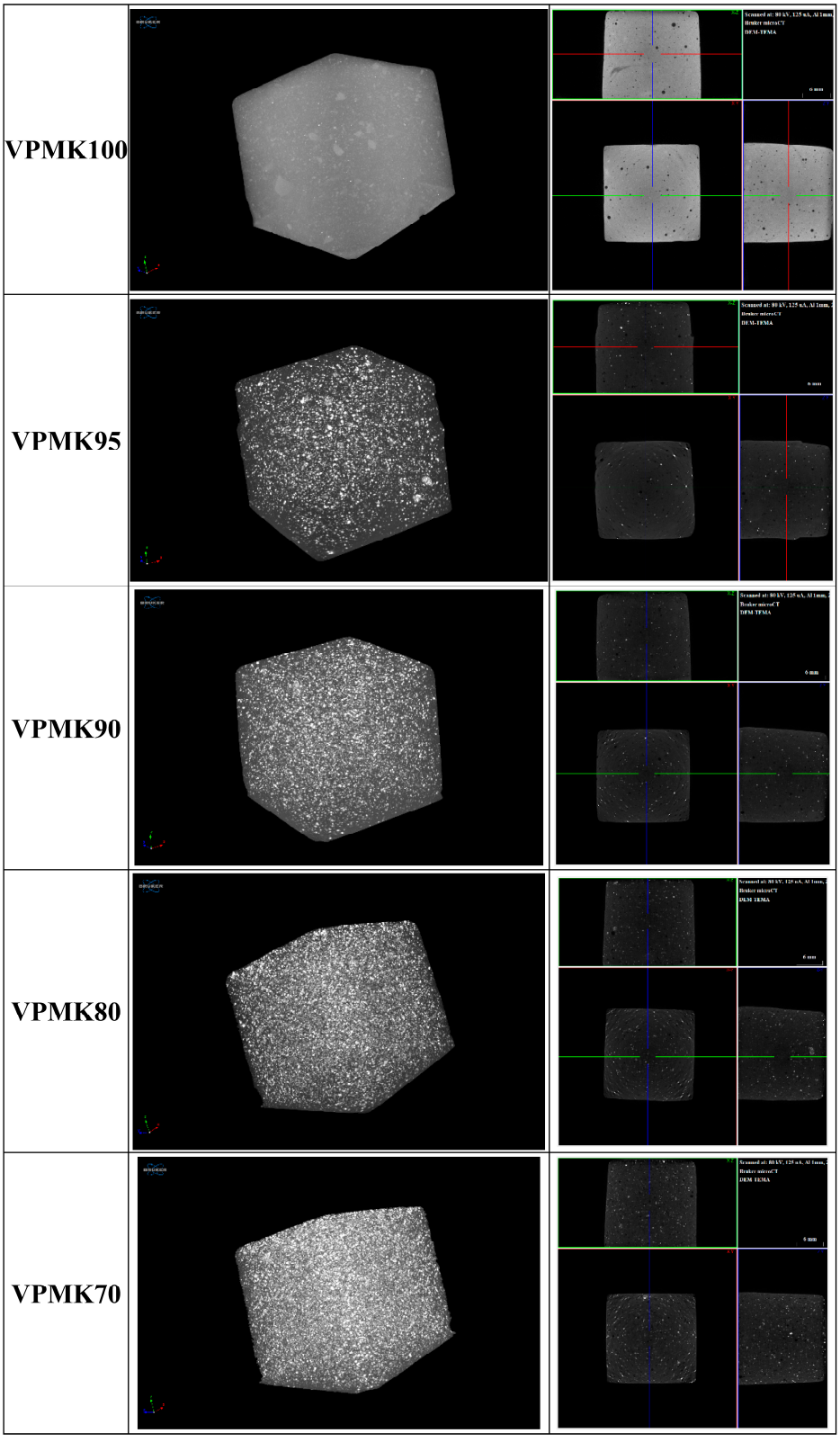

Figure 8. 3D micro-CT images of geopolymers.

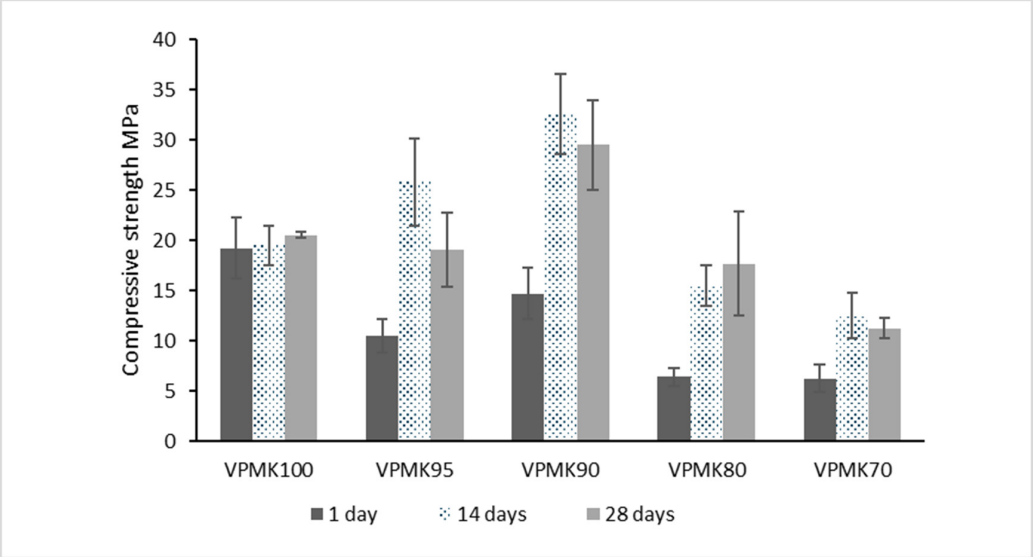

Figure 9. Compressive strength of geopolymers after 1, 14, and 28 days of curing. Error bars represent the standard deviation of triplicate measurements.

The SEM/EDS and micro-CT observations help explain this mechanical trend. SEM/EDS images of VPMK100, VPMK90, and VPMK70 (Figures 5–7) show that MW-derived mineral phases are incorporated within the geopolymer matrix, while micro-CT images (Figure 8) show a homogeneous three-dimensional distribution of denser particles within the geopolymer bodies. Therefore, the decrease in strength at higher MW contents does not appear to be related to major particle segregation but, rather, to the increasing proportion of MW-derived crystalline phases and the reduced continuity of the metakaolin-based geopolymer matrix. In this context, VPMK90 represents the most balanced formulation, combining effective MW incorporation with a compact and cohesive matrix, consistent with its highest compressive strength among the tested formulations (Figure 9).

The strength values obtained for VPMK95 (25 MPa) and VPMK90 (29.5 MPa) are higher than those of VPMK100 (20.5 MPa), which can be related to the high calcium content of the MW (CaO = 22.68 wt.%, Table 1). Under alkaline conditions, Ca^{2+} ions released from calcite and gypsum dissolution may contribute to the formation of C-S-H or C-A-S-H gels alongside the N-A-S-H geopolymer network, as reported for calcium-rich and slag-containing geopolymer systems [44,53,54]. The coexistence of these gel phases is known to improve matrix densification and mechanical performance [49,55]. Some observations in this study are consistent with this hypothesis: Fibrous particles seen by SEM in VPMK70 (Figure 6D) have a morphology often associated with C-S-H and C-A-S-H gels [48,49]. The micro-CT results (Figure 8) also show that VPMK90 has the densest matrix among all formulations, which supports the idea of a well-developed gel network at this MW content [52]. However, confirming C-S-H or C-A-S-H formation directly would require analyses not carried out in this study, such as FTIR, ^{29}Si MAS-NMR or TGA/DTG, which are recommended for future work.

The strength decrease observed for VPMK80 and VPMK70 is linked to gypsum dissolution under the alkaline conditions of geopolymerization (Equation (1)) [56,57]:

$$CaSO_4 \cdot 2H_2O + 2\ NaOH \rightarrow Ca(OH)_2 + Na_2SO_4 + 2\ H_2O. \quad (1)$$

This reaction affects the geopolymer system in three ways. First, two moles of NaOH are consumed per mole of gypsum, which reduces the amount of activator available

for metakaolin dissolution and gel formation [57]. Second, the Na_2SO_4 produced may precipitate in the pore network in an amorphous state below XRD detection limits, filling pore space and limiting gel development, as reported for similar gypsum-containing systems [57]. Third, the $Ca(OH)_2$ formed releases Ca^{2+} ions that, at low MW contents (5–10 wt.%), may contribute to C-S-H or C-A-S-H gel formation alongside the N-A-S-H network [44,49], which is consistent with the strength improvement seen for VPMK95 and VPMK90. At higher MW contents (20–30 wt.%), the loss of NaOH and pore filling by Na_2SO_4 become the dominant effects, leading to the progressive strength reduction observed for VPMK80 and VPMK70 (Figure 9).

However, VPMK90, VPMK80, and VPMK70 exhibited a declining strength trend from 14 to 28 days. Similar strength reductions have been reported in previous geopolymer studies and were attributed to shrinkage associated with pore drying during curing [57,58]. Since shrinkage, mass loss, porosity, and microcracking were not directly monitored in this study, this mechanism is considered a possible explanation.

The overall mechanical performance of VPMK90 is consistent with the SEM and micro-CT observations, which show that the 10 wt.% MW formulation presents a compact microstructure and well-integrated particle distribution within the geopolymer matrix.

2.3. Methylene Blue Adsorption

2.3.1. Effect of Contact Time

The dye adsorption capacities of the studied geopolymers over 120 min are presented in Figure 10. Among the MK-based geopolymers, both the VPMK100 and VPMK70 samples achieved 90% dye removal within 120 min. Most of the dye quantity was adsorbed within the initial 60 min, reaching equilibrium around the 90-min mark. Conversely, samples containing 5%, 10%, and 20% VPMK did not surpass 50% dye removal within the same contact time (Figure 11). The dye adsorption for VPMK100 and VPMK70 was of 22–23 mg/g, while the other samples adsorbed only 16 mg/g. The adsorption process seems tied to the availability of unoccupied surface sites for dye adsorption. The $[AlO_4]^{5-}$ tetrahedrons of the geopolymeric porous structure bear the capability to absorb cationic dyes due to the presence of surface hydroxyl groups. Once the available sites saturate, further adsorption ceases, reaching equilibrium [59,60].

Considering adsorption capacity and MB removal efficiency after 90 min, the sequence of geopolymer adsorbent performance is as follows: VPMK100 > VPMK70 (30% MW) > VPMK80 (20% MW) > VPMK90 (10% MW) > VPMK95 (5% MW).

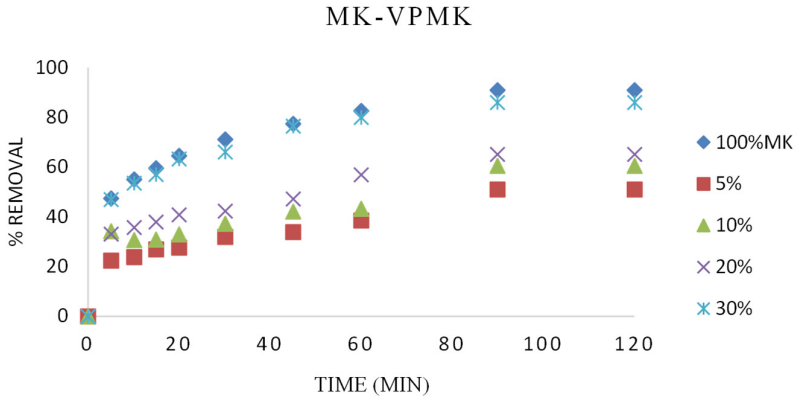

Figure 10. Contact time effect on the removal percentage of the methylene blue with 0.1 g of geopolymers and 12 ppm as MB concentration.

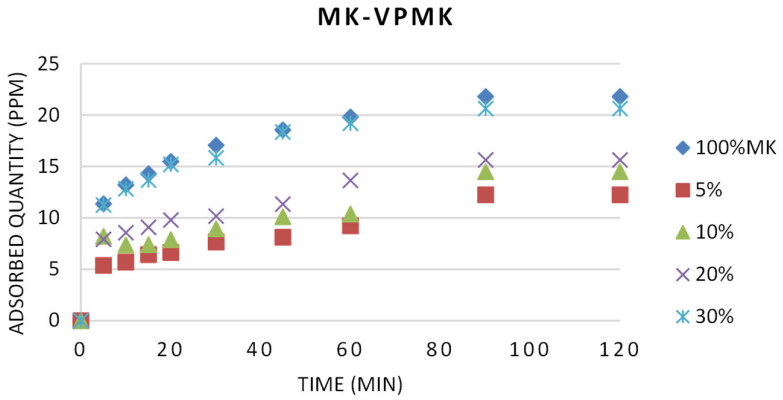

Figure 11. Contact time effect on the adsorbed quantity of the methylene blue with 0.1 g of geopolymers and 12 ppm as MB concentration.

2.3.2. Adsorption Isotherms

The results represented in the Langmuir and Freundlich isotherm plots (Figures 12 and 13) show that the R^2 value associated with the Langmuir isotherm model slightly surpasses that of the Freundlich model, suggesting that the adsorption of MB by the examined adsorbent corresponds more closely to the Langmuir isotherm model, indicating monolayer adsorption behavior. The Langmuir adsorption constant (K_L) serves as an indicator of the adsorbate–adsorbent interaction strength. A higher K_L value signifies a robust interaction between the adsorbate and adsorbent, whereas a smaller value suggests a weaker interaction. Among the samples, the 5%, 10%, and 20% VPMK exhibit the lowest K_L values, while the 100% VPMK, 30 wt.% VPMK, 5%, 10%, and 20% VPCMK demonstrate the highest values (Table 3). The equilibrium factor (R_L) derived from the Langmuir model assesses the adsorption process, with an R_L value between 0 and 1 indicating favorable adsorption. In this study, all R_L values remained below 1, signifying favorable adsorption of geopolymers. Additionally, a higher sludge content (30%VPMK) enhanced the adsorption process. For all formulations, 1/nF values range from 0.47 (VPMK95, 5% MW) to 0.97 (VPMK70, 30% MW), confirming favorable heterogeneous adsorption in which stronger binding sites are preferentially occupied first and binding energy decreases progressively with increasing surface coverage [61]. The corresponding n values (1.03 to 2.15, all within the range $1 < n < 10$) confirm favorable adsorption conditions across all formulations. The Langmuir isotherm provides a slightly better fit (R^2 = 0.997–0.999) than the Freundlich model (R^2 = 0.987–0.997) for all formulations, indicating that monolayer adsorption on the $[AlO_4]^{5-}$ binding sites is the dominant mechanism, while the Freundlich fit reflects the secondary contribution of heterogeneous surface sites introduced by the mineral phases of MW [29,59].

Table 3. Langmuir and Freundlich calculation results.

Sample	Slope ($1/q_{max}$)	Intercept	q_{max} (mg/g)	K_L (L/mg)	RL	R^2	Adsorption
VPMK100	0.0990	0.0012	10.10	82.50	0.00101	0.999	Favorable
VPMK95	0.0687	0.0101	14.56	6.80	0.01210	0.998	Favorable
VPMK90	0.0810	0.0076	12.35	10.66	0.00776	0.998	Favorable
VPMK80	0.0958	0.0047	10.44	20.38	0.00407	0.997	Favorable
VPMK70	0.1120	0.0004	8.93	280.00	0.00030	0.999	Favorable

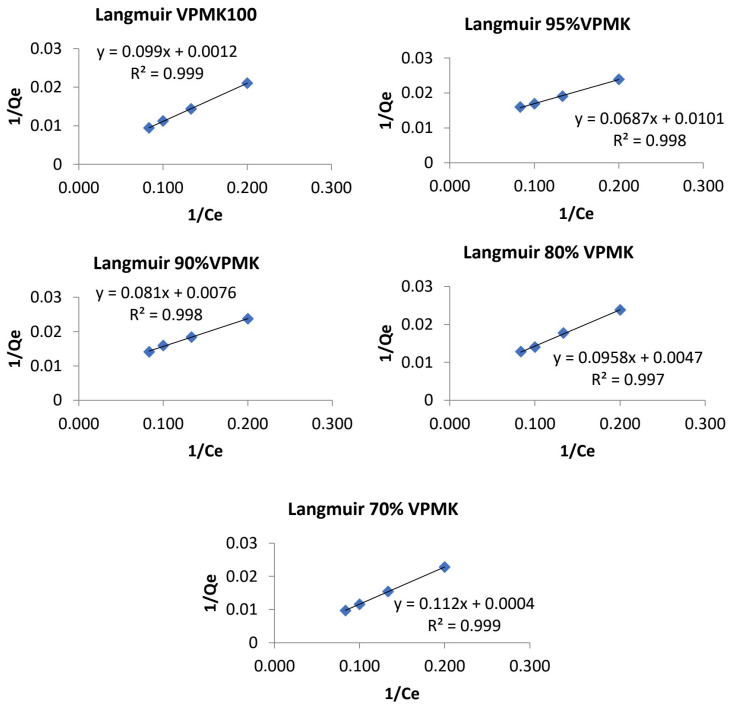

Figure 12. Langmuir isotherms of the MB adsorption.

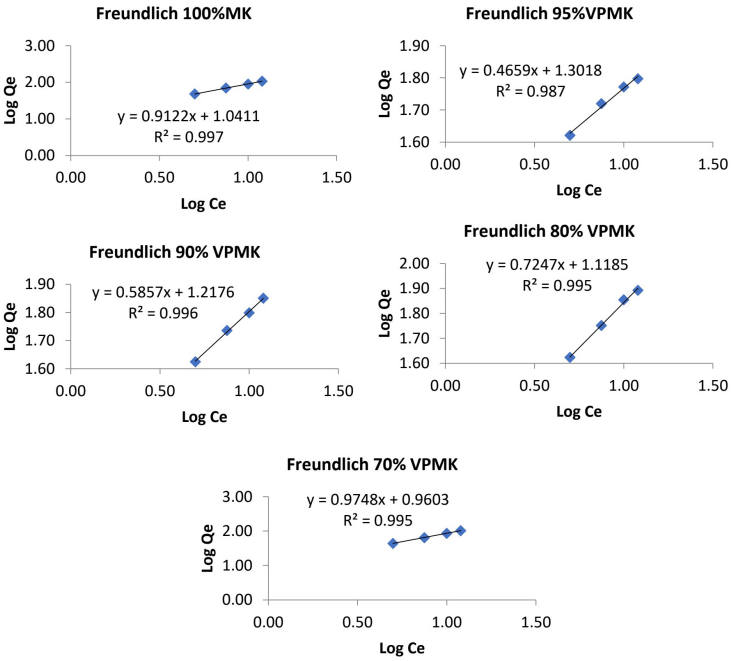

Figure 13. Freundlich isotherms of the MB adsorption.

2.3.3. Adsorption Kinetics

The experimental data were fitted with the pseudo-first-order (PFO) and pseudo-second-order (PSO) models. The corresponding parameters are presented in Table 4 and Figures 14 and 15. The R^2 values from the PFO model ranged from 0.566 to 0.931, and the calculated q_e values differed significantly from the experimental values, indicating that the PFO model does not describe MB adsorption well in these systems [62,63]. The PSO model gave a better fit for VPMK100 (R^2 = 0.994), VPMK80 (R^2 = 0.979), and VPMK70 (R^2 = 0.998), with good agreement between calculated and experimental q_e values. The lower PSO R^2 for VPMK90 (0.774) may reflect the dense and compact matrix of this formu-

lation, which introduces multi-stage diffusion kinetics not fully captured by a single-rate model [58,64]. The rate constant k_2 and the initial adsorption rate $h = k_2 \cdot q_e^2$, defined by Ho and McKay [62,65], provide useful information about how fast adsorption takes place in each formulation. In the PSO model, the rate is controlled by the availability of active sites on the surface rather than by the MB concentration in solution, which points to chemisorption as the main mechanism [62,66]. This is in line with the electrostatic interactions between the cationic MB molecule and the $[AlO_4]^{5-}$ sites of the N-A-S-H gel [63]. VPMK70 (30% MW) has the highest k_2 (0.01817 g/mg·min) and h (5.71 mg/g·min), meaning that adsorption starts fastest in this sample. This agrees with its high Langmuir affinity constant (KL = 280 L/mg, Table 3), which suggests that the mineral phases of MW galena and sphalerite surfaces identified by SEM/EDS (Figures 6B and 7B) provide high-energy sites that bind MB rapidly [29,65]. VPMK100 also shows a high initial rate (h = 3.12 mg/g·min), linked to the good accessibility of the $[AlO_4]^{5-}$ sites in the open pore structure of the pure metakaolin matrix [59,63]. VPMK90 (10% MW) provides the lowest k_2 (0.00249 g/mg·min) and h (0.476 mg/g·min), linked to its dense and compact matrix confirmed by micro-CT (Figure 8) and reflected in its highest compressive strength (29.5 MPa, Figure 9). The dense gel network limits MB diffusion to the internal binding sites, which slows the initial adsorption rate even though the total capacity remains reasonable (q_e = 13.83 mg/g). This is consistent with intraparticle diffusion theory, where pore structure controls how fast the adsorbate reaches the active sites [58,64]. The dense matrix responsible for the high mechanical strength of VPMK90 also slows down MB access to the binding sites. VPMK95 (k_2 = 0.00408 g/mg·min, h = 0.756 mg/g·min) and VPMK80 (k_2 = 0.00723 g/mg·min, h = 1.611 mg/g·min) fall between these two extremes. The increase in h from VPMK95 to VPMK80 and VPMK70 suggests that as MW content increases beyond 10 wt.%, the contribution of high-affinity mineral surfaces becomes more important and progressively increases the initial adsorption rate [29,65].

Although the incorporation of MW into the geopolymer matrix indicates potential for the immobilization of potentially toxic elements, the long-term environmental stability of these materials should be further validated through standardized leaching tests. Future studies should therefore include toxicity characteristic leaching procedures, EN 12457 batch leaching tests, pH-dependent leaching tests, and/or dynamic monolithic leaching tests to assess the mobility of Pb, Zn, Cd, As, and other trace elements after geopolymerization. Such protocols would allow evaluation of both crushed/granular material and monolithic geopolymer specimens under different exposure conditions. These tests are essential to confirm the effectiveness of the geopolymer matrix in reducing element release and to support the safe valorization of MW-based geopolymers in waste reuse and environmental remediation applications.

Table 4. The pseudo-first-order (PFO) and pseudo-second-order (PSO) models of MB adsorption with the studied geopolymers.

Sample	$q_e$exp (mg/g)	PFO q_e (mg/g)	PFO R^2	PSO q_e (mg/g)	k_2 (g/mg·min)	h (mg/g·min)	PSO R^2
VPMK100	17.83	10.36	0.566	18.87	0.00878	3.124	0.994
VPMK95	11.80	14.55	0.844	13.61	0.00408	0.756	0.949
VPMK90	12.56	9.85	0.761	13.83	0.00249	0.476	0.774
VPMK80	14.29	8.37	0.915	14.93	0.00723	1.611	0.979
VPMK70	17.25	20.68	0.931	17.73	0.01817	5.711	0.998

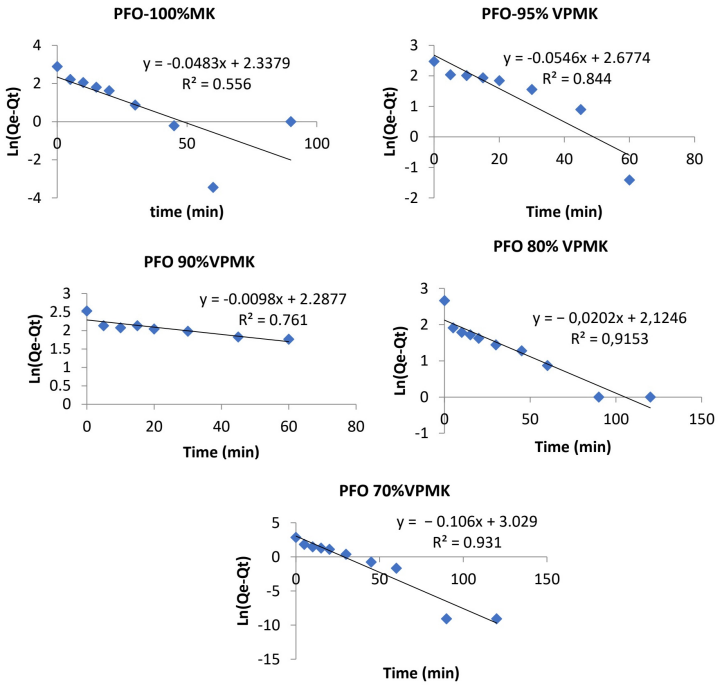

Figure 14. The pseudo-first-order (PFO) model.

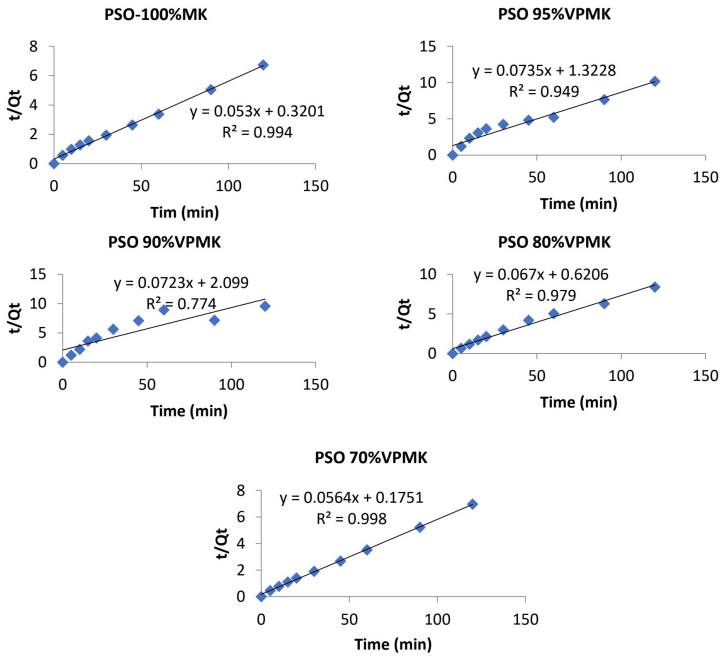

Figure 15. The pseudo-second-order (PSO) model.

3. Experimental Details

3.1. Materials

Mine waste (MW) was obtained from a Lakhouat mine, in the northwest of Tunisia. The site is located about 120 km south of the capital Tunis (Figure 16). Abandoned now, Lakhouat was a Pb-Zn district, exploited for almost a century using flotation technique since its discovery in 1892 until the exhaustion of the reserves in 1994 [3].

Five samples from the tailings at equal intervals from the top to the base of the storage site were collected and then mixed to obtain a representative sample. The sample underwent mechanical crushing and was then sieved to obtain a <125 µm fraction before geopolymer preparation. Finally, it was oven-dried at 50 °C for 48 h.

Vicente Pereira metakaolin (VPMK) prepared by calcination (700 °C/4 h) of kaolin from Vicente Pereira deposit, Ovar, Portugal, was used as aluminosilicate precursor for geopolymer preparation. More information about chemical and mineralogical composition of Vicente Pereira kaolin deposit is reported in [67].

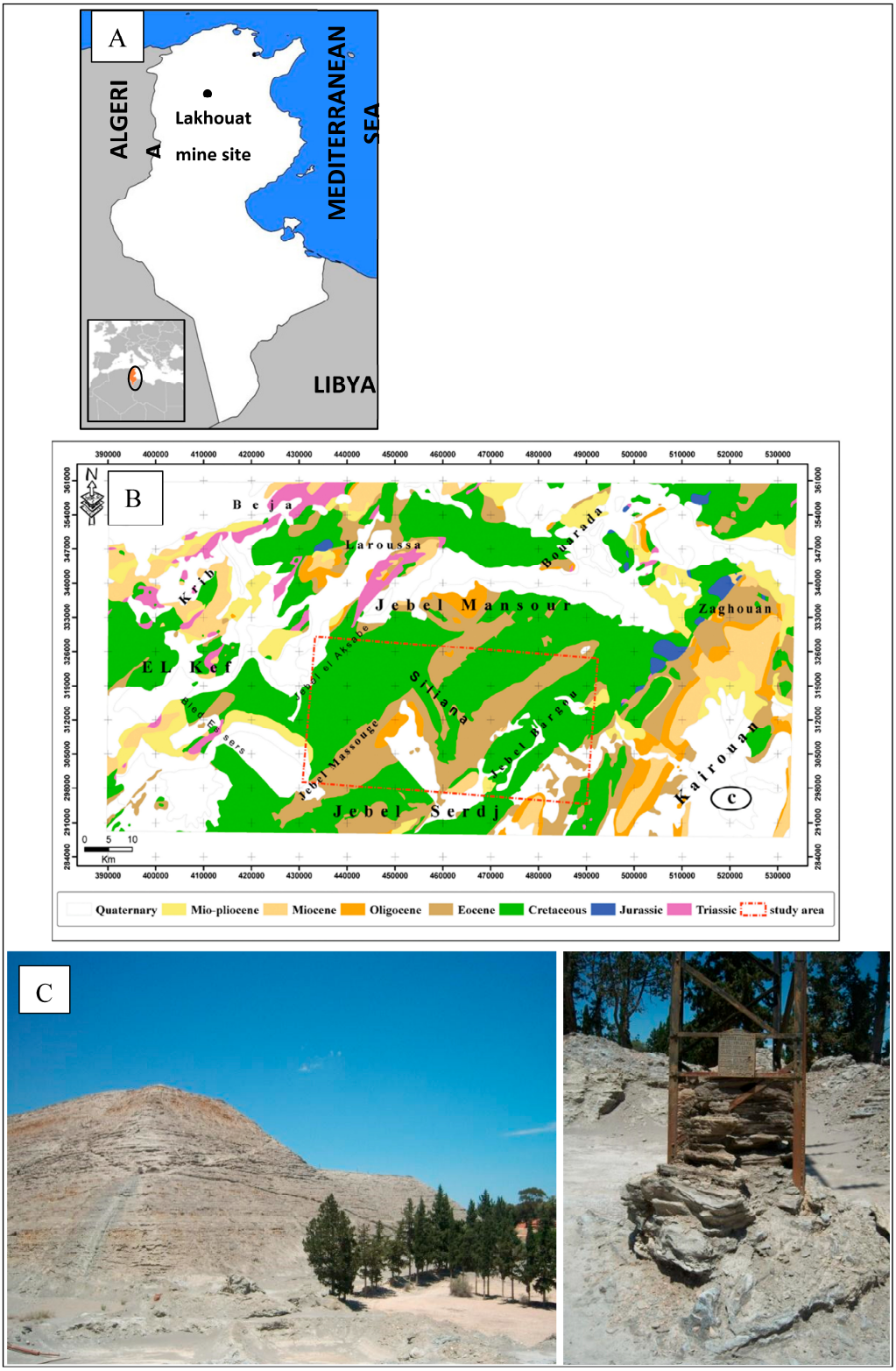

Figure 16. Location of the study area at different scales (**A**); localities bordering the study area (**B**), adapted from the 1/500 000 geological map of Tunisia [68]; and on-site photographs of mine waste tailings (**C**).

3.2. Methods

Particle size distribution of the metakaolin and MW was determined with an X-ray grain size analyzer, Sedigraph 5100, from Micromeritics (Norcross, GA, USA), following the Standard BS 3406-2 procedure [69]. Full-scale pump speed: 3; stir time: 60 s; stir speed: high; probe time: 30 s. MK density: 2.650 g/cm^3; MW density: 2.470 g/cm^3; liquid density: 0.9941 g/cm^3.

Mineralogical composition of raw materials and geopolymers was performed using X-ray diffraction instrument (Philips/Panalytical). The operating conditions were 30 mA and 50 kV using Cu Kα radiation (λ-1.5405 Å) with a speed of 0.02°/s and 2 s/step. The X-pert Highscore software (version 4.9 (2020) and the PDF-4 + 2023 database) were used to analyze XRD diffractograms.

X-ray fluorescence (XRF), conducted using a PANalytical Axios X-ray fluorescence spectrometer (PANalytical B.V., Almelo, The Netherlands), was used to analyze the chemical composition (major and trace elements) of the starting materials and produced geopolymers. Loss on ignition (LOI) was determined by heating the samples in an electrical furnace at 1000 °C during 3 h.

The surface morphology and microstructure of MW and geopolymers was performed by scanning electron microscopy, SEM-EDS (TESCAN VEGA, TESCAN ORSAY HOLDING, Brno, Czech Republic), with landing energy of 15 keV and beam current of 1 nA.

Micro-computed tomographic scans (micro-CT) of geopolymers were performed in X-ray 3D microtomograph (SkyScan 1275, Bruker microCT, Kontich, Belgium) with voltage of 20 kV, 175 μA current, and 450 ms exposure time.

The compressive strength was measured on triplicates of each geopolymer type on Precision Universal Tester equipment (AG-IC 100 kN, Shimadzu Corporation, Kyoto, Japan) by applying a maximum force of 5 kN at the speed of 50 N/s as per the standard EN 1015-11 [70].

Geopolymers preparation: MW was used as a low-cost mineral filler and partial substitute for metakaolin. Five types of geopolymers were prepared in which VPMK was replaced by 0, 5, 10, 20, and 30% of MW, entitled in the text as VPMK100, VPMK95, VPMK90, VPMK80, and VPMK70, respectively. Geopolymerization was carried out by mixing NaOH, Na_2SiO_3, and water. Hydrated sodium silicate (Merck, Darmstadt, Germany; 8.5 wt.% Na_2O, 28.5 wt.% SiO_2, 63 wt.% H_2O) and sodium hydroxide (ACS AR Analytical Reagent Grade Pellets) were used as alkaline activators in geopolymers preparation. The maximum MW replacement level investigated in this study was 30 wt.%. This value was selected as the upper limit of the experimental series in order to evaluate the effect of substantial MW incorporation while maintaining a comparable preparation protocol for all formulations. Higher MW contents were not investigated in the present work.

To produce geopolymers with lower environmental impact and reduced alkaline activator consumption, the formulation design followed the approach of Andrejkovičová et al. [71] and Sudagar et al. [72], using target SiO_2/Al_2O_3 and Na_2O/Al_2O_3 molar ratios of 1. For each MW replacement level, the amounts of sodium silicate, sodium hydroxide, and water were recalculated from the bulk oxide composition of the corresponding VPMK–MW blend in order to maintain comparable nominal formulation ratios across the series. The calculated H_2O/Na_2O ratios were kept below 20, with values of 9.60, 10.09, 11.67, 13.69, and 16.59 for VPMK100, VPMK95, VPMK90, VPMK80, and VPMK70, respectively. In geopolymer systems, the H_2O/Na_2O ratio is an important formulation parameter because it influences paste workability and may affect pore development and mechanical strength after curing. The SiO_2/Al_2O_3 and Na_2O/Al_2O_3 ratios should therefore be considered nominal bulk formulation ratios rather than exact reactive ratios available for N-A-S-H or calcium-containing gel formation because part of the Si, Al, Ca, S, Zn, and Pb in

MW occurs in crystalline phases with limited or uncertain reactivity. NaOH and hydrated sodium silicate were mixed in water and used to activate the aluminosilicate precursor. The obtained solution was added slowly to the metakaolin and MW with agitation by a Heidolph ST1 laboratory stirrer (Heidolph Instruments, Schwabach, Germany)at two different speeds (100 rpm for 2 min and 200 rpm for 4 min) to avoid the formation of gases and agglomerations and to ensure optimum homogeneity. The pastes were immediately poured into 20 × 20 × 20 mm cubic molds, vibrated for 5 min to release bubbles, and cured at laboratory temperature for up to 28 days.

Methylene blue was selected as a widely used model cationic dye to provide a preliminary screening of the adsorption potential of the synthesized MW-MK geopolymers and to allow comparison with previous geopolymer-based adsorbent studies. The geopolymers were milled before adsorption testing to increase the accessible surface area, reduce diffusion limitations, and evaluate the intrinsic adsorption potential of the material. Methylene blue MB adsorption tests were performed as follows:

For adsorption, 0.1 g of milled geopolymer was added to 200 mL of methylene blue trihydrate solution (MB; CAS No. 7220-79-3; Thermo Fisher Scientific, supplied by VWR International, Radnor, Pennsylvania, USA) with initial MB concentrations of 12, 10, 7.5, and 5 ppm and magnetically stirred for 2 h at room temperature. Aliquots from the solution were taken at regular time intervals, and the MB concentration in the liquid was evaluated by determining the absorbance in a spectrometer (Shimadzu UV-3100, Kyoto, Japan) at a l ¼ 664 nm.

The amount of MB adsorbed by the powdered geopolymer samples was calculated using Equation (2):

$$q_e = (C_0 - C_e) \times V/m \quad (2)$$

where q_e is the quantity of MB uptake by the geopolymer (mg MB/g geopolymer), C_0 is the initial concentration of MB (mg/L), C_e is the remaining equilibrium MB concentration (mg/L), V is the solution volume (L), and m is the mass of geopolymer (g).

The removal efficiency (E) of the dye was determined using Equation (3):

$$E(\%) = \frac{C_i - C_e}{C_i} \times 100 \quad (3)$$

Langmuir and Freundlich adsorption isotherm models were used to fit the experimental results [73]. The Langmuir model assumes homogeneous binding sites and equivalent sorption energies in the surface and that there is no interaction between the sorbed species [73]. It is described by the equation:

$$\frac{t}{q_e} = \frac{1}{q_m} + \frac{1}{K_L q_m C_e} \quad (4)$$

In Equation (4), K_L (L/mg) is the affinity of the sorbate for the binding sites; q_{max} (mg/g) is the maximum adsorption capacity. Once the K_L value is obtained, the Langmuir isotherm can be expressed by a separation factor, R_L, given by:

$$R_L = \frac{1}{1 + K_L C_0} \quad (5)$$

If R_L is between 0 and 1, then there is favorable adsorption.

The Freundlich isotherm model, on the other hand, has been interpreted as sorption onto a heterogeneous surface, which is a site that can have varying affinity. In that model,

one presumes that the stronger binding sites are occupied first and that the binding strength decreases with an increasing degree of occupation [73]. The model has the form:

$$q_e = K_F C_e^{1/n} \quad (6)$$

where K_F is the Freundlich constant, and n is a parameter which represents the absence of linearity of the adsorbed quantity in function of C_e. Equation (6) is usually converted into alternative linear form, thus becoming:

$$\log q_e = \log K_f + \left(\frac{1}{n}\right) \log C_e \quad (7)$$

If the value of n is between 1 and 10, then there is favorable adsorption. Larger values of n suggest, on the contrary, a stronger interaction between the surface of the adsorbent and adsorbate; when 1/n is equal to 1, this indicates a linear adsorption, leading to identical adsorption energies for all the sites [74].

4. Conclusions

This study presents a method of recycling Lakhouat Tunisian Pb-Zn mine waste (MW) through geopolymer formulation with varying MW proportions (0, 5, 10, 20, and 30 wt.%). This research aligns with the circular economy by showcasing how geopolymers made with industrial waste can address environmental pollutants. Key findings are as follows:

- The characterization of MW reveals a bimodal particle size distribution and a mineral composition rich in carbonates and sulfides. High concentrations of PTEs, such as those found in lead (2.23 wt.%), zinc (8.2 wt.%), cadmium, arsenic, nickel, and chromium, raise environmental concerns. This underscores the need for effective management and reuse strategies to mitigate impacts and enhance sustainability in mining.
- Incorporating MW into the geopolymer matrix results in a heterogeneous yet cohesive material, enhancing its microstructural complexity. SEM and EDS analyses reveal diverse mineral phases, including sphalerite and galena, which suggest effective integration of MW minerals.
- Tomography images of all formulated geopolymers demonstrate a consistent and homogeneous distribution of particles, highlighting the effective integration of MW. Notably, even with increasing percentages of MW, results showed the uniformity of particle distribution.
- Compressive strength results indicate that VPMK90, containing 10 wt.% MW, represents the optimum formulation among the tested mixtures, reaching the highest strength, ≈30 MPa, after 28 days of curing. This performance is consistent with the compact microstructure observed by SEM and the homogeneous particle distribution shown by micro-CT, suggesting that moderate MW incorporation improves the balance between waste valorization and mechanical performance.
- Higher MW contents led to a reduction in compressive strength, probably due to dilution of the reactive metakaolin fraction, increased contribution of crystalline phases from MW, and possible sulfate-related effects that may hinder geopolymer gel development. The strength decline observed from 14 to 28 days for VPMK70, VPMK80, and VPMK90 may also be related to pore shrinkage and microstructural changes during curing.
- MB adsorption tests show that VPMK100 and VPMK70 (30% MW) reached removal efficiencies above 90% within 120 min, with adsorption capacities of 22–23 mg/g. The Langmuir model gave a better fit (R^2 = 0.997–0.999) than the Freundlich model

(R^2 = 0.987–0.997), suggesting monolayer adsorption on the $[AlO_4]^{5-}$ sites of the geopolymer framework. The pseudo-second-order model gave the best fit for the kinetics ($R^2 \geq 0.949$ for VPMK100, VPMK80, and VPMK70), pointing to chemisorption as the rate-controlling step. VPMK70 showed the highest adsorption affinity (K_L = 280 L/mg) and fastest initial rate (h = 5.71 mg/g·min), while VPMK90 had the lowest initial rate (h = 0.476 mg/g·min); this result was linked to its dense matrix, which was confirmed by micro-CT.

Author Contributions: Conceptualization, J.N., S.A. and F.R.; methodology, J.N., S.A., O.K. and F.R.; software, T.P., R.R. and G.G.; validation, J.N., S.A., T.P., R.R. and F.R.; formal analysis, O.K., S.A., T.P., R.R., and G.G.; investigation, J.N., O.K., T.P. and R.R.; resources, A.C., M.G. and F.R.; data curation, J.N., O.K., T.P. and R.R.; writing—original draft preparation, J.N.; writing—review and editing, J.N., S.A., O.K., A.C., M.G. and F.R.; visualization, J.N.; supervision, F.R., S.A., A.C. and M.G.; project administration, J.N. and F.R.; funding acquisition, A.C., M.G. and F.R. All authors have read and agreed to the published version of the manuscript.

Funding: This research was funded by the GeoBioTec Research Unit (UIDB/04035/2020), the Training and Research in Italian Laboratories (TRIL) Programme at OGS and ICTP, the Deep Blue Project—Developing Education and Employment Partnerships for a Sustainable Blue Growth in the Western Mediterranean Region (European Maritime and Fisheries Fund and the European Agency for Small and Medium-sized Enterprises, Grant No. EASME/EMFF/2017/1.2.1.12/S3/02, Project No. SI2.789633), and the Islamic Development Bank (IsDB) Scholarship Programme, Grant No. 2019-1610760. The APC was funded by the National Institute of Oceanography and Applied Geophysics (OGS).

Data Availability Statement: The data presented in this study are available within the article. Additional data supporting the findings of this study are available from the corresponding author upon reasonable request.

Acknowledgments: This work was supported by: GeoBioTec research unit (UI/04035/2020); Training and Research in Italian Laboratories Program (TRIL) at OGS and ICTP; Deep Blue project coordinated by OGS ICAP—Developing Education and Employment Partnerships for a Sustainable Blue Growth in the Western Mediterranean Region (European Maritime and Fishery Fund and European Agency for Small and Medium-sized enterprises within the framework of the Sustainable Blue Economy Call 2017 (easme/emff/2017/1.2.1.12/s3/02/si 2.789633) and ISDB 2019-1610760 Scholarship.

Conflicts of Interest: The authors declare no conflicts of interest.

References

1. Altiti, A.H.; Alrawashdeh, R.O.; Alnawafleh, H.M. Open pit mining. In *Mining Methods*; IntechOpen: London, UK, 2021. [CrossRef]
2. Marín, O.A.; Kraslawski, A.; Cisternas, L.A. Estimating processing cost for the recovery of valuable elements from mine tailings using dimensional analysis. *Miner. Eng.* **2022**, *184*, 107629. [CrossRef]
3. Nouairi, J.; Baraud, F.; Leleyter, L.; Mefteh, S.; Rocha, F.; Medhioub, M. Spatial distribution and ecological risk assessment of potentially toxic elements in agricultural soils, stream sediments, and plants around Lakhouat mine (northwestern Tunisia). *Arab. J. Geosci.* **2021**, *14*, 130. [CrossRef]
4. Chaabani, S.; Abdelmalek-Babbou, C.; Ben Ahmed, H.; Chaabani, A.; Sebei, A. Phytoremediation assessment of native plants growing on Pb–Zn mine site in Northern Tunisia. *Environ. Earth Sci.* **2017**, *76*, 585. [CrossRef]
5. Daldoul, G.; Souissi, R.; Tlil, H.; Elbahri, D.; El Hamiani, O.; Chebbi, N.; Boularbah, A.; Souissi, F. Assessment of heavy metal toxicity in soils contaminated by a former Pb–Zn mine and tailings management using flotation process, Jebel Ghozlane, Northern Tunisia. *Environ. Earth Sci.* **2019**, *78*, 703. [CrossRef]
6. Othmani, M.A.; Souissi, F.; da Silva, E.F.; Coynel, A. Accumulation trends of metal contamination in sediments of the former Pb–Zn mining district of Touiref (NW Tunisia). *J. Afr. Earth Sci.* **2015**, *111*, 231–243. [CrossRef]
7. Sliti, N.; Abdelkrim, C.; Ayed, L. Assessment of tailings stability and soil contamination of Kef Ettout (NW Tunisia) abandoned mine. *Arab. J. Geosci.* **2019**, *12*, 73. [CrossRef]
8. El Kateb, A.; Stalder, C.; Rüggeberg, A.; Neururer, C.; Spangenberg, J.E.; Spezzaferri, S. Impact of industrial phosphate waste discharge on the marine environment in the Gulf of Gabes (Tunisia). *PLoS ONE* **2018**, *13*, e0197731. [CrossRef]

9. Hentati, O.; Abrantes, N.; Caetano, A.L.; Bouguerra, S.; Gonçalves, F.; Römbke, J.; Pereira, R. Phosphogypsum as a soil fertilizer: Ecotoxicity of amended soil and elutriates to bacteria, invertebrates, algae and plants. *J. Hazard. Mater.* **2015**, *294*, 80–89. [CrossRef]
10. Mlayah, A.; Ferreira da Silva, E.; Rocha, F.; Ben Hamza Ch Charef, A.; Noronha, F. The Oued Mellègue: Mining activity, stream sediments and dispersion of base metals in natural environments, north-western Tunisia. *J. Geochem. Explor.* **2009**, *102*, 27–36. [CrossRef]
11. Nouairi, J.; Rocha, F.; Medhioub, M. Geobiological assessment of the pollution effect of abandoned mine ores (Fej Lahdoum, Northwest Tunisia). *Arab. J. Geosci.* **2019**, *12*, 806. [CrossRef]
12. Srarfi, F.; Rachdi, R.; Bol, R.; Gocke, M.I.; Brahim, N.; SlimShimi, N. Stream sediments geochemistry and the influence of flood phosphate mud in mining area, Metlaoui, Western south of Tunisia. *Environ. Earth Sci.* **2019**, *78*, 211. [CrossRef]
13. Ayari, J.; Agnan, Y.; Charef, A. Spatial assessment and source identification of trace metal pollution in stream sediments of Oued El Maadene basin, northern Tunisia. *Environ. Monit. Assess.* **2016**, *188*, 397. [CrossRef]
14. Ayari, J.; Barbieri, M.; Barhoumi, A.; Boschetti, T.; Braham, A.; Dhaha, F.; Charef, A. Trace metal element pollution in media from the abandoned Pb and Zn mine of Lakhouat, Northern Tunisia. *J. Geochem. Explor.* **2023**, *247*, 107180. [CrossRef]
15. Mseddi, H.; Ben Mammou, A. Contamination assessment of Remir and Siliana stream sediments by El Akhouat mine discharges (Siliana basin, North-western of Tunisia). *Geo-Eco-Trop* **2014**, *38*, 305–316.
16. Sahraoui, H.; Hachicha, M. Caractérisation de la contamination spatiale par le Pb, Zn et Cd de l'ancienne mine de Lakhouat (Siliana, Tunisie). *J. Nat. Sci.* **2016**, *9*, 2286–5314.
17. Aiguobarueghian, I.; Adanma, U.M.; Ogunbiyi, E.O.; Solomon, N.O. Waste management and circular economy: A review of sustainable practices and economic benefits. *World J. Adv. Res. Rev.* **2024**, *22*, 1708–1719. [CrossRef]
18. Bouzar, B.; Mamindy-Pajany, Y. Immobilization study of As, Cr, Mo, Pb, Sb, Se and Zn in geopolymer matrix: Application to shooting range soil and biomass fly ash. *Int. J. Environ. Sci. Technol.* **2023**, *20*, 11891–11912. [CrossRef]
19. Castillo, H.C.; Droguett, T.; Sánchez, S.; Vesely, M.; Garrido, P.; Palma, S. Factors affecting the compressive strength of geopolymers: A review. *Minerals* **2021**, *11*, 1317. [CrossRef]
20. Mabroum, S.; Moukannaa, S.; El Machi, A.; Taha, Y.; Benzaazoua, M.; Hakkou, R. Mine wastes based geopolymers: A critical review. *Clean. Eng. Technol.* **2020**, *1*, 100014. [CrossRef]
21. Nagaraju, T.V.; Mantena, S.; Gobinath, R.; Bonthu, S.; Subhan Alisha, S. Geopolymer-stabilized soils: Influencing factors, strength development mechanism and sustainability. *J. Taibah Univ. Sci.* **2023**, *17*, 2248651. [CrossRef]
22. Wong, L.S. Durability performance of geopolymer concrete: A review. *Polymers* **2022**, *14*, 868. [CrossRef]
23. Chen, Z.; Yu, J.; Nong, Y.; Yang, Y.; Zhang, H.; Tang, H. Beyond time: Enhancing corrosion resistance of geopolymer concrete and BFRP bars in seawater. *Compos. Struct.* **2023**, *322*, 117439. [CrossRef]
24. Al-Fakih, A.; Mohammed, B.S.; Wahab, M.M.A.; Liew, M.S.; Mugahed Amran, Y.H. Recent progress in geopolymer concrete technology: A review. *Iran. J. Sci. Technol. Trans. Civ. Eng.* **2024**, *48*, 3285–3308. [CrossRef]
25. Asghar, R.; Ali Khan, M.; Alyousef, R.; Javed, M.F.; Ali, M. Promoting the green construction: Scientometric review on the mechanical and structural performance of geopolymer concrete. *Constr. Build. Mater.* **2023**, *368*, 130502. [CrossRef]
26. Pobłocki, K.; Pawlak, M.; Drzeżdżon, J.; Gawdzik, B.; Jacewicz, D. Clean production of geopolymers as an opportunity for sustainable construction development. *Sci. Total Environ.* **2024**, *928*, 172579. [CrossRef] [PubMed]
27. Tochetto, G.A.; Simão, L.; de Oliveira, D.; Hotza, D.; Immich, A.P.S. Porous geopolymers as dye adsorbents: Review and perspectives. *J. Clean. Prod.* **2022**, *374*, 133982. [CrossRef]
28. Jin, H.Z.; Qiu, C.X.; Li, Y.S.; Liu, B.; Liu, J.Y.; Chen, Q.; Lu, X.F.; Li, C.X.; Wang, Q.K. Structural and functional design of geopolymer adsorbents: A review. *Tungsten* **2024**, *6*, 48–76. [CrossRef]
29. Siyal, A.A.; Shamsuddin, M.R.; Khan, M.I.; Rabat, N.I.; Zulfiqar, M.; Man, Z.; Siame, J.; Azizli, K.A. A review on geopolymers as emerging materials for the adsorption of heavy metals and dyes. *J. Environ. Manag.* **2018**, *224*, 327–339. [CrossRef]
30. Khan, S.; Malik, A. Environmental and health effects of textile industry wastewater. In *Environmental Deterioration and Human Health: Natural and Anthropogenic Determinants*; Malik, A., Grohmann, E., Akhtar, R., Eds.; Springer: Dordrecht, The Netherlands, 2014; pp. 55–71. [CrossRef]
31. Pendy, H.N.; Tiwari, S.C.; Tripathi, M.M. Insecticides and herbicides. In *Environmental Biotechnology*; APH Publishing Corporation: New Delhi, India, 2007; pp. 313–335.
32. Rafatullah, M.; Sulaiman, O.; Hashim, R.; Ahmad, A. Adsorption of methylene blue on low-cost adsorbents: A review. *J. Hazard. Mater.* **2010**, *177*, 70–80. [CrossRef]
33. Banerjee, S.; Gautam, R.K.; Jaiswal, A.; Chattopadhyay, M.C.; Sharma, Y.C. Rapid scavenging of methylene blue dye from a liquid phase by adsorption on alumina nanoparticles. *RSC Adv.* **2015**, *5*, 14425–14440. [CrossRef]
34. Gupta, V.K.S. Application of low-cost adsorbents for dye removal—A review. *J. Environ. Manag.* **2009**, *90*, 2313–2342. [CrossRef] [PubMed]
35. Souissi, R.; Souissi, F.; Chakroun, H.K.; Bouchardon, J.L. Mineralogical and geochemical characterization of mine tailings and Pb, Zn, and Cd mobility in a carbonate setting (Northern Tunisia). *Mine Water Environ.* **2013**, *32*, 16–27. [CrossRef]

36. Fabbri, B.; Gualtieri, S.; Leonardi, C. Modifications induced by the thermal treatment of kaolin and determination of reactivity of metakaolin. *Appl. Clay Sci.* **2013**, *73*, 2–10. [CrossRef]
37. Middleton, A.P.; Edwards, H.G.M.; Middleton, P.S.; Ambers, J. Identification of anatase in archaeological materials by Raman spectroscopy: Implications and interpretation. *J. Raman Spectrosc.* **2005**, *36*, 984–987. [CrossRef]
38. Barbosa, V.; Hernani, M.; Bráulio, M. Assessing risks of abandoned urban mines in the UNESCO World Heritage City of Ouro Preto, Brazil. *Appl. Geogr.* **2022**, *139*, 102648. [CrossRef]
39. Cánovas, C.R.; Dino, Q.; Francisco, M.C.B.; Arias-Borrego, A.; García-Barrera, T.; Nieto, J.M. Potential release and bioaccessibility of metal/loids from mine wastes deposited in historical abandoned sulfide mines. *Environ. Pollut.* **2023**, *316*, 120629. [CrossRef]
40. Villa Gomez, D.; Sáez Salgado, E.; Mejías, O.; Pat-Espadas, A.M.; Pinedo Torres, L.A.; Jackson, L.; Parbhakar-Fox, A. Data integration of critical elements from mine waste in Mexico, Chile and Australia. *Minerals* **2022**, *12*, 122. [CrossRef]
41. Elgarahy, A.M.; Maged, A.; Eloffy, M.G.; Zahran, M.; Kharbish, S.; Elwakeel, K.Z.; Bhatnagar, A. Geopolymers as sustainable eco-friendly materials: Classification, synthesis routes, and applications in wastewater treatment. *Sep. Purif. Technol.* **2023**, *324*, 124631. [CrossRef]
42. Merabtene, M.; Kacimi, L.; Clastres, P. Elaboration of geopolymer binders from poor kaolin and dam sludge waste. *Heliyon* **2019**, *5*, e01938. [CrossRef]
43. Kouamo Tchakouté, H.; Rüscher, C.H.; Hinsch, M.; Yankwa Djobo, J.N.; Kamseu, E.; Leonelli, C. Utilization of sodium waterglass from sugar cane bagasse ash as a new alternative hardener for producing metakaolin-based geopolymer cement. *Geochemistry* **2017**, *77*, 257–266. [CrossRef]
44. García-Lodeiro, I.; Palomo, A.; Fernández-Jiménez, A.; Macphee, D.E. Compatibility studies between N-A-S-H and C-A-S-H gels. Study in the ternary diagram Na_2O–CaO–Al_2O_3–SiO_2–H_2O. *Cem. Concr. Res.* **2011**, *41*, 923–931. [CrossRef]
45. Richardson, I.G. The calcium silicate hydrates. *Cem. Concr. Res.* **2008**, *38*, 137–158. [CrossRef]
46. Provis, J.L.; Bernal, S.A. Geopolymers and related alkali-activated materials. *Annu. Rev. Mater. Res.* **2014**, *44*, 299–327. [CrossRef]
47. Van Deventer, J.S.J.; Provis, J.L.; Duxson, P. Technical and commercial progress in the adoption of geopolymer cement. *Miner. Eng.* **2012**, *29*, 89–104. [CrossRef]
48. Tang, W.; Pignatta, G.; Sepasgozar, S.M.E. Life-cycle assessment of fly ash and cenosphere-based geopolymer material. *Sustainability* **2021**, *13*, 11167. [CrossRef]
49. Richardson, I.G. Model structures for C-(A)-S-H(I). *Acta Crystallogr. Sect. B* **2014**, *70*, 903–923. [CrossRef]
50. Liu, J.; Wen, S.; Xian, Y.; Deng, J.; Huang, Y. Dissolubility and surface properties of a natural sphalerite in aqueous solution. *Min. Metall. Explor.* **2012**, *29*, 113–120. [CrossRef]
51. Bao, Z.; Al, T.; Couillard, M.; Poirier, G.; Bain, J.; Shrimpton, H.K.; Finfrock, Y.Z.; Lanzirotti, A.; Paktunc, D.; Saurette, E.; et al. A cross scale investigation of galena oxidation and controls on mobilization of lead in mine waste rock. *J. Hazard. Mater.* **2021**, *412*, 125130. [CrossRef]
52. Chung, S.-Y.; Kim, J.-S.; Stephan, D.; Han, T.-S. Overview of the use of micro-computed tomography (micro-CT) to investigate the relation between the material characteristics and properties of cement-based materials. *Constr. Build. Mater.* **2019**, *229*, 116843. [CrossRef]
53. Kumar, S.; Kumar, R.; Mehrotra, S.P. Influence of granulated blast furnace slag on the reaction, structure and properties of fly ash based geopolymer. *J. Mater. Sci.* **2010**, *45*, 607–615. [CrossRef]
54. Shi, C.; Krivenko, P.V.; Roy, D. *Alkali-Activated Cements and Concretes*; Taylor & Francis: London, UK, 2006.
55. García-Lodeiro, I.; Fernández-Jiménez, A.; Palomo, A.; Macphee, D.E. Effect of calcium additions on N-A-S-H cementitious gels. *J. Am. Ceram. Soc.* **2010**, *93*, 1934–1940. [CrossRef]
56. Taylor, H.F.W. *Cement Chemistry*, 2nd ed.; Thomas Telford: London, UK, 1997.
57. Prasanphan, S.; Onutai, S.; Nawaukkaratharnant, P. Influence of partial replacement of calcined red clay by gypsum-bonded casting investment waste on geopolymerization reaction of red clay-based geopolymer. *Heliyon* **2024**, *10*, e24448. [CrossRef]
58. Karoui, O.; Andrejkovičová, S.; Pato, P.; Patinha, C.; Řimnáčová, D.; Perná, I.; Hajjaji, W.; Rocha, F.; Mlayah, A. Foamed phosphate by-product based geopolymers and dye adsorption efficiency. *Appl. Clay Sci.* **2024**, *257*, 107446. [CrossRef]
59. Falah, M.; MacKenzie, K.J.D.; Knibbe, R.; Page, S.J.; Hanna, J.V. New composites of nanoparticle Cu(I) oxide and titania in a novel inorganic polymer (geopolymer) matrix for destruction of dyes and hazardous organic pollutants. *J. Hazard. Mater.* **2016**, *318*, 772–782. [CrossRef]
60. Lee, J.W.; Choi, S.P.; Thiruvenkatachari, R.; Shim, W.G.; Moon, H. Evaluation of the performance of adsorption and coagulation processes for the maximum removal of reactive dyes. *Dyes Pigments* **2006**, *69*, 196–203. [CrossRef]
61. Dada, A.O.; Olalekan, A.P.; Olatunya, A.M.; Dada, O.J.I. Langmuir, Freundlich, Temkin and Dubinin–Radushkevich isotherms studies of equilibrium sorption of Zn^{2+} unto phosphoric acid modified rice husk. *IOSR J. Appl. Chem.* **2012**, *3*, 38–45.
62. Ho, Y.S.; McKay, G. Pseudo-second order model for sorption processes. *Process. Biochem.* **1999**, *34*, 451–465. [CrossRef]
63. Li, L.; Wang, S.; Zhu, Z. Geopolymeric adsorbents from fly ash for dye removal from aqueous solution. *J. Colloid. Interface Sci.* **2006**, *300*, 52–59. [CrossRef]
64. Weber, W.J., Jr.; Morris, J.C. Kinetics of adsorption on carbon from solution. *J. Sanit. Eng. Div.* **1963**, *89*, 31–60. [CrossRef]

65. Ho, Y.S.; McKay, G. The kinetics of sorption of divalent metal ions onto sphagnum moss peat. *Water Res.* **2000**, *34*, 735–742. [CrossRef]
66. Largitte, L.; Pasquier, R. A review of the kinetics adsorption models and their application to the adsorption of lead by an activated carbon. *Chem. Eng. Res. Des.* **2016**, *109*, 495–504. [CrossRef]
67. Santos, A.; Andrejkovičová, S.; Almeida, F.; Rocha, F. Thermoelectric properties of geopolymers with iron ore mine waste: A case study for energy management. *Ceram. Int.* **2024**, *50*, 36112–36125. [CrossRef]
68. Ben Haj Ali, M.; Jédoui, Y.; Dali, T.; Ben Salem, H.; Memmi, L. *Carte Géologique 1/500000 de la Tunisie*; Service Géologique, Office National des Mines: Tunise, Africa, 1985.
69. *BS 3406-2*; Methods for Determination of Particle Size Distribution—Part 2, Recommendations for Determination of Particle Size Distribution by Sedimentation Methods. British Standards Institution: London, UK, 1986.
70. *EN 1015-11*; Methods of Test for Mortar for Masonry—Part 11, Determination of Flexural and Compressive Strength of Hardened Mortar. European Committee for Standardization (CEN): Brussels, Belgium, 1999.
71. Andrejkovičová, S.; Sudagar, A.; Rocha, J.; Patinha, C.; Hajjaji, W.; Ferreira da Silva, E.; Velosa, A.; Rocha, F. The effect of natural zeolite on microstructure, mechanical and heavy metals adsorption properties of metakaolin based geopolymers. *Appl. Clay Sci.* **2016**, *126*, 141–152. [CrossRef]
72. Sudagar, A.J.; Andrejkovičová, S.; Rocha, F.; Patinha, C.; Soares, M.R.; Velosa, A.L.; da Silva, E.F. Combined influence of low-grade metakaolins and natural zeolite on compressive strength and heavy metal adsorption of geopolymers. *Minerals* **2021**, *11*, 486. [CrossRef]
73. LeVan, M.D.; Vermeulen, T.J. The adsorption of organic compounds on activated carbon. *J. Phys. Chem.* **1981**, *85*, 3247–3250. [CrossRef]
74. Febrianto, F.; Royama, L.I.; Hidayat, W.; Bakar, E.S.; Kwon, J.H.; Kim, N.H. Development of oriented strand board from acacia wood (*Acacia mangium* Willd.): Effect of pretreatment of strand and adhesive content on the physical and mechanical properties of OSB. *J. Korean Wood Sci. Technol.* **2009**, *37*, 121–127.